UNIVERSITY OF OKLAHOMA

GRADUATE COLLEGE

A PRIORI TESTING OF SUBGRID-SCALE MODELS FOR LARGE EDDY SIMULATIONS IN SUPERSATURATED CONDITIONS

A THESIS

SUBMITTED TO THE GRADUATE FACULTY

in partial fulfillment of the requirements for the

Degree of

MASTER OF SCIENCE

By

KENDRA GILLIS

Norman, Oklahoma

2023

A PRIORI TESTING OF SUBGRID-SCALE MODELS FOR LARGE EDDY SIMULATIONS IN SUPERSATURATED CONDITIONS

A THESIS APPROVED FOR THE

SCHOOL OF METEOROLOGY

BY THE COMMITTEE CONSISTING OF

Dr. Scott Salesky, Chair

Dr. Raymond Shaw

Dr. Otavio Costa Acevedo

Acknowledgements

I would like to thank NSF, grant OIA-1929124, for funding and supporting this research.

I would like to thank Michigan Technology University for their collaboration and allowing us to use their Pi Chamber for our experiments. I would like to thank those who work with the Pi Chamber, especially Dr. Raymond Shaw and Ian Helman, for helping me understand the cloud chamber and understand turbulence throughout the entirety of this research.

I would also like to thank my parents for their encouragement and constant support. They've always been there to help me in any way they could, from late night rants to pictures of forgotten notes. I never could have made it here without them. And I would like to thank my brothers and sisters for their endless patience and support.

And thank you to those at the University of Oklahoma who were there to assist with homework, programming and everything else these past three years have thrown at me. I never could have made it through without you.

Thank you.

Table of Contents

List of Tables

List of Figures

Abstract

Turbulence is characterized by irregular movement in pressure and flow velocity. Better understanding of turbulent flow will help in the understanding of air movement including wind currents, dissipation of pollutants and storm formation. Although much research has been done on the nature of turbulence in the atmosphere, less work has been focused on humidity turbulence in supersaturated conditions. Supersaturation turbulence is found in clouds and plays a major role in the formation of precipitation. In an effort to better understand LES and the closure problem for turbulence fluctuations of supersaturation, temperature was monitored within a cloud chamber while turbulence was being induced. Several measurements were made with a thermistor array at various temperature differences and spacings. The data gathered was used for a priori testing. Two models, a scale-similarity model and a Gradient model, were tested with the data gathered. The scale-similarity showed to be very promising with correlation coefficients around 0.7. The Gradient model had correlation coefficients around 0.2. Although one of the models performed slightly better at the smallest horizontal spacing, there didn't appear to be any significant patterns between horizontal spacing or temperature difference and how well the models performed. A posteriori tests will need to be performed in the future to better test how well the scale-similarity model behaves in various circumstances. Supersaturation LES models will further scientists' understanding of the humidity turbulence present during the formation of clouds and precipitation.

Chapter 1

Introduction

1.1: Turbulent Flow

Turbulent flow is when the attributes of the flow (e.g. temperature, momentum, saturation) are irregular rather than consistent. In turbulent flow, fluids undergo irregular flow patterns which induce mixing. Turbulent flow is characterized by many swirling eddies (Pope, 2000). Often, when turbulence is studied, it is done so in reference to these eddies. If the swirling motion of a turbulent fluid can be understood or modeled, the overall motion of the turbulence can be understood and modeled. For this reason, much of studying turbulence begins with studying the large-scale and small-scale swirling motion (Sagaut, 2001).

The largest of these eddies is often the size of the barrier the flow is interacting with. The eddies get increasingly smaller until it is deemed molecular motion instead of kinetic motion.

The Navier-Stokes equations are equations originally crafted in the 1800s showing the motion and momentum of turbulent flow (equation 1). They are based on conservation of mass, Newton's second law and the assumption that stress in the fluid is the sum of the diffusing viscous term and pressure term. However, they are not completely integrable (Pope, 2000). In order to use the Navier-Stokes, the fluid

must be treated as a continuous substance, ignoring the properties of individual molecules.

$$\frac{\partial u_i}{\partial t} + u_j \frac{\partial u_i}{\partial x_j} = -\frac{1}{\rho}\frac{\partial p}{\partial x_i} + \nu \frac{\partial^2 u_i}{\partial x_j^2} \qquad \text{(equation 1)}$$

Though the Navier-Stokes equations are accurate, the larger the area of turbulence being simulated and the more complex that turbulence is, the more computationally expensive simulations become. Most turbulent flows that scientists are interested in, especially meteorologists, are fairly large. Storms can easily reach 25 kilometers in diameter, or larger. This means, when cloud formation or storms need to be numerically simulated, options are limited.

The most straightforward method is direct numerical simulation (DNS). This is when the Navier-Stokes equations are used for the entire system. The fluid is treated as a continuous system and even the finest turbulent eddies are resolved for every time step. Understandably, a supercomputer must be used to perform even the smallest of numerical simulations. The amount of computational power needed is enormous. Because of this, scientists developed the method of large eddy simulation.

LES, large eddy simulation, is a combination of the Navier-Stokes equations and statistical analyses. As addressed earlier, turbulence is made of many swirling eddies. In LES, these flows are divided into grid-scale turbulence and subgrid-scale turbulence. The grid-scale turbulence is the larger, more regular flow which is

simulated explicitly. The subgrid-scale turbulence is not simulated but rather it is modeled using statistics and models crafted from experimental data. The grid-scale turbulence is then simulated using a variation of the Navier-Stokes equations which takes the statistics of the modeled, less periodic flow into account.

$$\frac{\partial \widetilde{u_i}}{\partial t} + \widetilde{u_j}\frac{\partial \widetilde{u_i}}{\partial x_j} = -\frac{1}{\rho}\frac{\partial \tilde{p}}{\partial x_i} + \nu\frac{\partial^2 \widetilde{u_i}}{\partial x_j^2} - \frac{\partial \tau_{ij}}{\partial x_j} \qquad \text{(equation 2)}$$

In this variation of the Navier-Stokes momentum equation (equation 2), the coefficients expressing pressure and movement are altered to represent the average over larger areas. The term that represents dissipation of energy to viscosity, is negligible at the high Reynolds numbers found in turbulent flow. It is replaced with a term that represents dissipation of energy into subgrid eddies. It is this variable which is referred to as the subgrid scale stress tensor, because it is a representation of how the turbulent energy behaves on a subgrid scale.

LES is computationally reasonable and gives valuable and reliable results. However, its accuracy is dependent on the accuracy of the subgrid-scale model.

The basis of most of these subgrid-scale models still used in LES is the Smagorinsky model (Smagorinsky, 1963). This simple model was proposed by Smagorinsky in 1963. It's a linear eddy-viscosity model (generally represented with $\boldsymbol{\tau}$) used to relate the residual stress to the filtered rate of strain. Equation 3 shows the equation for this τ.

$$\tau_{ij}^{r} = -2v_r\widetilde{S_{ij}} \qquad \text{(equation 3)}$$

$$v_r = l_S^2\tilde{S} = (C_S\Delta)^2\tilde{S} \qquad \text{(equation 4)}$$

v_r is the eddy viscosity of the residual motion. v_r is found by multiplying the characteristic filtered rate of strain by the Smagorinsky length scale squared (equation 4). The Smagorinsky length scale is the product of the filter width and the Smagorinsky coefficient (equation 4). In the Smagorinsky model, and all models based off of it, energy transfer occurs everywhere from the filtered motions to the residual motions. Also, there is no backscatter, meaning energy and momentum are never modeled to come up from the subgrid-eddies to create more grid-scale eddies (Smagorinsky, 1963).

Smagorinsky's model is still recognized by many as the original functional LES model (equation 5).

$$v_t = (C_S\Delta)^2\left(\widetilde{S_{ij}}\widetilde{S_{ij}}\right)^{1/2} \qquad \text{(equation 5)}$$

However, models have been developed since to try to compensate for its shortcomings. In the Smagorinsky model, the Smagorinsky coefficient can change drastically depending on the Reynolds number. This means that fluid flowing near a wall is simulated with a different coefficient than fluid flowing in the center, even

though all other factors are the same. Inconsistencies like this can make it difficult to simulate an entire system with a single LES (Sagaut, 2001).

In 1991, Germano et al. attempted to fix this shortcoming by proposing the dynamic model (Germano et al. 1991). The dynamic method tries to overcome this difficulty by having two filters of different filter widths, the grid LES filter and the test LES filter. One shortcoming of the eddy viscosity subgrid-scale stress models used in large-eddy simulation at the time was their inability to represent, with a single universal constant, different turbulent fields. These flows included rotating and shear flows, near solid walls and in transitional regimes. Germano et al. suggested a new eddy viscosity model which would alleviate many of these drawbacks. The model coefficient was computed dynamically as the calculation progressed, rather than input a priori. The model was based on an algebraic identity between the subgrid-scale stresses at two different filtered levels and the resolved turbulent stresses. The subgrid-scale stresses obtained using the proposed model vanished in laminar flow and at a solid boundary, and had the correct asymptotic behavior in the near-wall region of a turbulent boundary layer. The results of large-eddy simulations of transitional and turbulent channel flow that used the proposed model were in good agreement with the direct simulation data.

In 1980, Bardina, Ferziger and Reynolds proposed a model often called the scale-similarity model. In this model, the stress term is decomposed into the Leonard stress, the cross stress and the SGS Reynolds stress. Because the large-scale

velocity is known, Leonard stress can be evaluated. After analyzing various models for the subgrid-scale turbulence, they came to the conclusion that there was enough information in the resolved scales to allow some of the characteristics of the complete flow field to be determined. They decomposed the kinetic energy of the small-scale motions into two parts: correlated and uncorrelated. From this, they crafted a two-component eddy-viscosity model. They found that the “production equals dissipation” argument did not hold for the small scales in the decay of turbulence because it did not account for the uncorrelated component. If the two-component model is reduced to a single-component model, similar to the ones that had been used previously, it shows many of the same flaws as the previous models did. Their model was based on the argument that the exchange between the large and small scales takes place mainly between the smallest of the large scales and the largest of the small scales. They also proposed a new length scale for use with anisotropic filters (Bardina, 1980).

All of these models were crafted in an effort to better represent the statistically relevant motion of the subgrid-scale models. If the effect of the subgrid turbulence can be accurately represented, simulations can be made for large scale fluid flows, such as clouds and storms, with much greater accuracy. This will help scientists better understand the nature of turbulence and how it changes in different circumstances. This will also help meteorologists better foresee and predict storms, precipitation and changes in weather.

1.2: Forming Models for LES

First, a model of subgrid motion is conceived for a particular turbulent flow. In many equations the model is referred to as τ (see equation 2). Generally, the model is based on knowledge of fluid mechanics and small-scale turbulence. However, there are variables and coefficients in the model which remain unknown. In order to find the value of these, scientists perform a priori testing (Meneveau, 2000). Data is gathered from either DNS or laboratory experiments of the same configuration the model was designed for. The subgrid-scale data is then filtered out and used to calculate $\tau_{calculated}$. $\tau_{calculated}$ is compared to the modeled τ. Through this comparison, it can be found mathematically what the best values for the coefficients and variables are. Through this a priori testing, the model, τ, can then be completed.

In order to form and test models for LES, it is required that both a priori and a posteriori testing are done. A priori testing is done first. It is the calculation of subgrid-scale models using data from DNS or experimentation. After the models are validated, a posteriori testing is performed. This is the implementation of the subgrid-scale model into LES and the comparison of the data provided by the model to the data shown in experimentation. A similar method has been used in many other papers including Sullivan et al. (2003), Porté-Agel et al. (2001), Keating (2004) and Kleissl, et al. (2003).

Traditionally, Low-Reynolds-number DNS is used for SGS model evaluation (Ma, 2011). This is because it contains the necessary three-dimensional spatial

information to generate SGS fluxes and resolved field gradients. The ability to acquire multi-dimensional turbulence data in laboratory and field studies has, however, improved sufficiently allowing a priori testing to be performed with high Reynolds number measurements. There are many suggested SGS closures for LES, but not all have been thoroughly tested. In the Sullivan et al. paper, the HATS (The Horizontal Array Turbulence Study) dataset was used to evaluate aspects of SGS models typical of those implemented in working LES of the PBL, many of which were eddy-viscosity-based parameterizations (Sullivan, 2018).

It should be noted that a priori tests, as shown in this paper, are only a first step in judging a SGS model. A posteriori tests with LES are required to ascertain the full interactions between resolved motions and the model. Good performance of an SGS model in a priori tests does not always translate into acceptable LES.

After the model is developed, it is combined with the filtered Navier-Stokes equations to create an LES (see equation 2). A posteriori tests are then performed to test how well the model works. The LES is compared statistically to turbulence data gathered from DNS or laboratory testing of similar configuration to what the model was designed for. Through a posteriori testing, it can be seen how well the model works when applied to the simulation.

All of these models, therefore, are based on applying an appropriate filtering system. There are many ways to filter turbulence into subgrid-scale and grid-scale

turbulence. The filtering types used in this research involve converting the turbulence measured to wavenumber space using the Fourier transform.

Data is transformed into spectral space which shows the frequency of the eddies. The frequency spectrum is put through a filter. Then, the filtered frequency spectrum is taken through the inverse Fourier transform. The result is the representation of the grid-scale turbulence (See figure 1). Eddies with frequencies that are not filtered out will be simulated. But the eddies with frequencies that are filtered out must be modeled with τ.

There are several ways to filter turbulence in spectral space. The first is the box filter. This takes the turbulence in wavenumber space and cuts it off at a certain frequency. This has the effect of taking the average of pockets of turbulence and so "smoothing it out." However, though the turbulence is cut-off sharply in physical space, it adds a slight oscillation to the turbulence data in spectral space. Often, this slight oscillation is inconsequential, but it can lead to inaccurate interpretations if analysts are not careful.

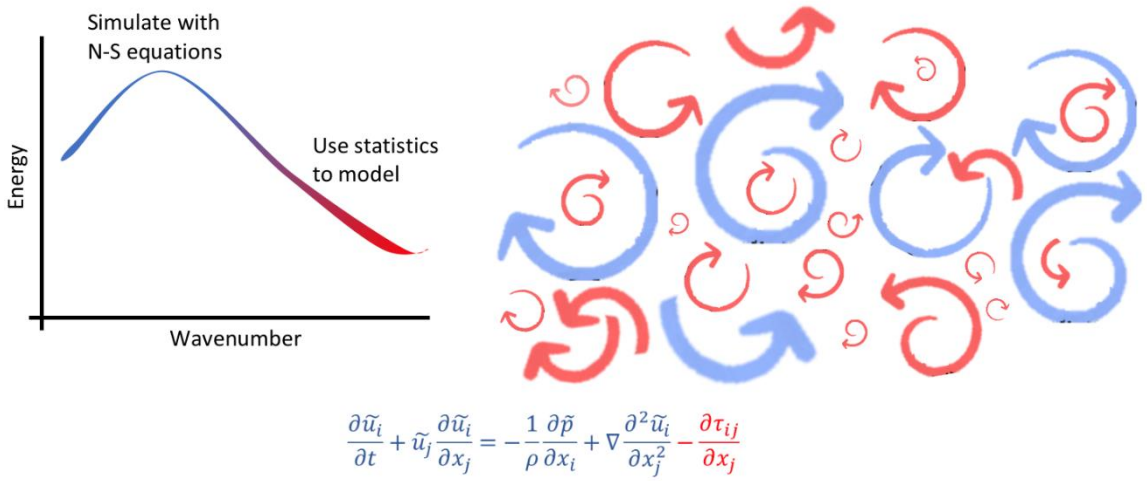

Figure 1. On the right is shown a representation of swirling eddies in turbulence. On the left is a graph of the turbulence in wave space. In this example, the red eddies are being modeled while the blue eddies are being simulated. The red portion of the line on the wavenumber versus energy graph shows what wavenumbers are being modeled and which are being simulated. The red portion of the line corresponds to the red eddies, which have higher frequency. This is also shown on the equation on the bottom. The blue portions of the equations calculate the simulated eddies while the red term is the model term.

In an effort to eliminate the oscillatory effects of the box filter in spectral space, the sharp-spectral filter was proposed. This gives a sharp cut-off in spectral space, which can make it easier to analyze and work with. However, this means the turbulence is not averaged in the same way in physical space.

The third common filter is a filter which tries to balance averaging out the spectral space and the physical space. This is the Gaussian filter. This filters the data through a Gaussian curve in spectral space. Unlike previous filters, there is not a dramatic suppression of high-wavenumber components, but rather a gradual cut-

off. This filter is often chosen as the best one to use when analysts are interested in the behavior of turbulence both in spectral space and physical space.

Many other filters are used, but these are the three most common (Pope, 2000). Though they are each trying to represent a separation of grid-scale and subgrid-scale turbulence, it is difficult to know which one truly represents real-world outcomes the best. The different filters work better depending on what model you are using them for. Each has their advantages and disadvantages, which is why it is advisable to do a priori testing with multiple of them.

1.3: Turbulence in Clouds

Clouds are localized areas of saturated or supersaturated air. Due to lifting, the air has reached its dew point and the water has begun to condense. Because of this, the density of clouds is higher than the surrounding air. Often clouds form around frontal passages, mountain wave activity, thermals, temperature inversions and other atmospheric disturbances (Wyngaard, 1992). Taking these things into account, it is easy to see why the flow of fluids in clouds is different, and generally more turbulent, than in clear skies.

Clouds form when an air pocket that is saturated or close to saturated is lifted and cooled. This is generally caused by a combination of atmospheric behavior and topography. The moisture in the air pocket condenses from a large volume into a

relatively small volume of rain, snow, hail and sleet. As water droplets form, potential energy is converted into kinetic and thermal energy. This creates eddies and swirling motions of varying sizes and intensities throughout clouds.

It is highly important in studying weather and climate to understand the interactions of aerosols, cloud droplets, ice crystals and trace gasses within the atmosphere. Many of these interactions happen within clouds. Therefore, the study of the internal workings of clouds is of great significance to the meteorology community. However, what remains especially vexing is that clouds are constantly in a state of turbulence (Bodenschatz, E., et al., 2010). Therefore, thermodynamic and compositional variables, such as water vapor supersaturation, fluctuate in space and time.

Turbulence often arises from buoyant forces, mechanical forces or some combination of the two. It is how a fluid in the atmosphere efficiently transports heat, mass and momentum as more kinetic and thermal energy is added to the system. The rate at which energy is being transferred from larger eddies to smaller eddies and then down to viscosity is often considered the intensity of the turbulence (Silva, 2014). LES has been used to study this cloud turbulence for over thirty years now (Deardorf, 1980).

It has been found that, on shorter time scales, fluctuations in supersaturation are generated by turbulent fluctuations of temperature and water vapor concentration (Siebert, 2017). It's also been shown that turbulence plays a large role in precipitation formation in clouds (Devenish, 2012), especially in the initiation of

warm rain in cumulus clouds (Grabowski, 2013). A substantial part of rain droplet formation is collision and coalescence. This is the process of smaller droplets being whipped around and running into each other, which would be heightened in a more turbulent environment. Thermodynamic and fluid-mechanical interactions between droplets and the surrounding air also play a large role in microscale properties in clouds, which affects the clouds interactions with atmospheric radiation and chemicals (Shaw, 2003). Therefore, to better understand cloud behavior, it is important to understand many types of turbulence within supersaturated conditions.

The presence of two prominent variables in cloud turbulence, humidity and temperature, makes it more complicated than most turbulence simulated. For the temperature ranges considered in this paper, it has been found that the water vapor's contribution to buoyancy is overpowered by the thermal contribution (Chandrakar, 2018). Therefore, we will be focusing on studying thermal turbulence induced by a difference in temperature.

Furthermore, supersaturation turbulence in clouds plays a large role in the creation of precipitation. In a paper done by Siebert and Shaw in 2017, it was mathematically shown that the variance of temperature and variance of water vapor are large contributors in supersaturation variance (Siebert, 2017). In most Rayleigh-Benard turbulence, variations in temperature are strongly correlated with variations in supersaturation. This suggests that it is likely possible to use turbulent temperature

fluctuations as a viable replacement for turbulent supersaturation fluctuations under certain conditions. This will allow the community to better simulate the formation of precipitation in clouds.

1.4: Pi Chamber at Michigan Tech

There is a cloud chamber at Michigan Technology University (Michigan Tech) known as the Pi Chamber. Due to its cylindrical wall boundary having a diameter of 2 meters and a height of 1 meter, it has an inner, working volume of 3.14 m^3 (hence the name). In the cloud chamber at Michigan Tech, turbulence is induced by heating the floor and cooling the ceiling, thus creating Rayleigh-Benard turbulence (see figure 2).

This Pi chamber is capable of pressures ranging from 1,000 to -60hPa. It can sustain temperatures from -55°C to 55°C, which spans the temperature range of most tropospheric clouds. Through aerosol generators, droplets ranging from 5μm to 40μm can be added to the chamber. This induces cloud growth. Through the manipulation of these variables, the Pi Chamber can produce clouds in a controlled environment which are very close to clouds found in nature (Cheng, 2016). Turbulent humidity fluctuations are measured with an open-path gas analyzer (Licor LI7500) which gives the average over a ~10 cm path. (Anderson, 2021)

The difference in temperature between the floor and the ceiling is what creates turbulence in the Pi chamber. The air close to the floor is warmed and so begins to rise. The ceiling is kept at a cooler temperature than the floor. When the air reaches the ceiling, it cools and so begins to sink. This constant upward and downward motion generates turbulence. The turbulence created is made up of eddies of varying sizes, including a large eddy roughly the size of the Pi Chamber. This is the dominant circulation in the Pi Chamber (Anderson et al., 2021). It can be monitored using resistance temperature detectors (RTDs) and a sonic anemometer.

This chamber has been used in many experiments and has been the center of many papers over the past seven years. Its ability to control variables such as temperature and humidity makes it invaluable when studying cloud behavior. When used with RTDs, lasers and other measuring devices, the Pi chamber has given much insight into cloud turbulence and how to model it.

Experiments can be run for both dry and wet conditions. Wet conditions are created by moistening a paper lining on both the ceiling and the floor. Wet conditions are further divided into moist and cloudy conditions. In cloudy conditions, there is the presence of sodium chloride aerosol particles which, if supersaturated conditions are achieved, lead to cloud droplet formation. They are not present for moist conditions.

In 2018, a paper was published showing the effects of various variables on turbulence in the clouds formed in the Pi chamber (Niedermeier, 2018). In the study,

both small-scale and large-scale flow properties of turbulent Rayleigh-Benard convection were investigated. It was found that the addition of water vapor influenced the turbulent flow. In all cases, the turbulent kinetic energy dissipation rate increased with increasing temperature difference, but the slopes were different for wet and dry convection. No clear difference between moist and cloudy conditions was observed. It was believed that this was due to low liquid water content which did not allow for complete cloud formation. Similar variations were found with the first normalized characteristic oscillation frequency which increased with increasing temperature difference and changed slope shape between wet and dry conditions but not between moist and cloudy conditions. It would appear that the sloshing or torsional mode of the large-scale circulation and the turbulent flow or energy dissipation rate seems to be influenced by the same mechanism additional to the effect of buoyancy alone. These observational results provide supporting evidence that the large-scale circulation is insensitive to phase composition or interfacial physics and rather depends only on the strength of the turbulence.

Recently, the Pi Chamber has been involved in several cutting-edge experiments and research developments (Desai, 2018; Thomas, 2019). Something that has long been considered as a mechanism for bridging the cloud droplet growth gap between condensation and collision–coalescence is diffusional growth of droplets by stochastic condensation and a resulting broadening of the size distribution. Some studies have shown that fluctuations in supersaturation can lead to changes in droplet size distribution at the condensational stage of droplet growth. However, few

studies took into account possible fluctuations in the phase relaxation time of a cloud parcel. To help better understand these possible oversights, the Pi Chamber was used to study steady-state cloud conditions. Clouds were created under monitored conditions and digital inline holography was used to directly observe the variations in local number concentration and droplet size distribution. It was found that the variability in integral radius is primarily driven by variations in the droplet number concentration and not the droplet radius (Desai, 2018).

The Pi Chamber at Michigan Tech offers the opportunity to study aerosol-cloud microphysics interactions in a turbulent environment with minimal changes to controlling variables such as mean temperature and mean humidity. In 2019, an experiment was run in which an atmospheric large-eddy simulation (LES) model with spectral bin microphysics was scaled down to simulate these interactions, allowing comparison with experimental results. To explore the effects of sidewalls on the bulk mixing temperature, water vapor mixing ratio and supersaturation, a simple scalar flux budget model was developed. The LES dynamics results were then compared to image velocimetry measurements from the Pi chamber. The simulated results and experimental results matched quantitatively. This suggests that the LES used is able to simulate steady-state cloud conditions and broadening of the cloud droplet size distribution with decreasing droplet number concentration, as was done in the experiments. This opened a path for further detailed intercomparison of laboratory and simulation results for model validation and exploration of specific physical processes (Thomas, 2019).

1.5: Purpose of Research

Although potential LES subgrid models have been researched for many types of turbulence, it was generally done in dry air. There has been little research into models for LES in saturated and supersaturated air. However, understanding and modeling turbulence in supersaturated air is necessary (Brinkop, 1995). Turbulence plays a large role in cloud behavior and precipitation formation as precipitation is often stimulated and grown through turbulent behavior (Devenish, 2012). So, it is important to know how to model turbulence in saturated environments.

Turbulent fluctuations of supersaturation are difficult to measure. They are, however, closely correlated to turbulent fluctuations of temperature (Chandrakar, 2020). Temperature is a much easier scalar to measure than supersaturation. In this research, the turbulent temperature fluctuations are measured using thermistors. The humidity fluctuation is also measured using the instrumentation in the Pi Chamber, though not as delicately. It is measured over a path, which is different than temperature which is averaged at a point.

Calculating models with greater accuracy for turbulent temperature fluctuations in saturated air will greatly improve the community's ability in modeling the development of clouds. This will help in the forecasting of precipitation and storms and in furthering the understanding of cloud formation and behavior.

Chapter 2

Methods

2.1: Experiments Within the Pi Chamber

Naturally occurring clouds are large, complex and high above the surface. They can, therefore, be very difficult to study directly. However, clouds can be formed and then studied in laboratory settings. The most common way to do this is with a cloud chamber. Cloud chambers can form clouds under many different conditions that naturally exist, and some that do not naturally exist, in the atmosphere. In these cloud chambers, clouds can be formed at different temperatures and different aerosol levels, and can be sustained for long periods of time. This makes it possible to study long-term averaging in what would naturally be unstable conditions.

There is a particular cloud chamber at Michigan Tech University (MTU) known as the Pi Chamber. Due to its cylindrical wall boundary having a diameter of 2 meters and a height of 1 meter, it has an inner, working volume of 3.14 m^3 (hence the name). In the cloud chamber at MTU, turbulence is induced by heating the floor and cooling the ceiling, thus creating thermal turbulence (Chang, 2016).

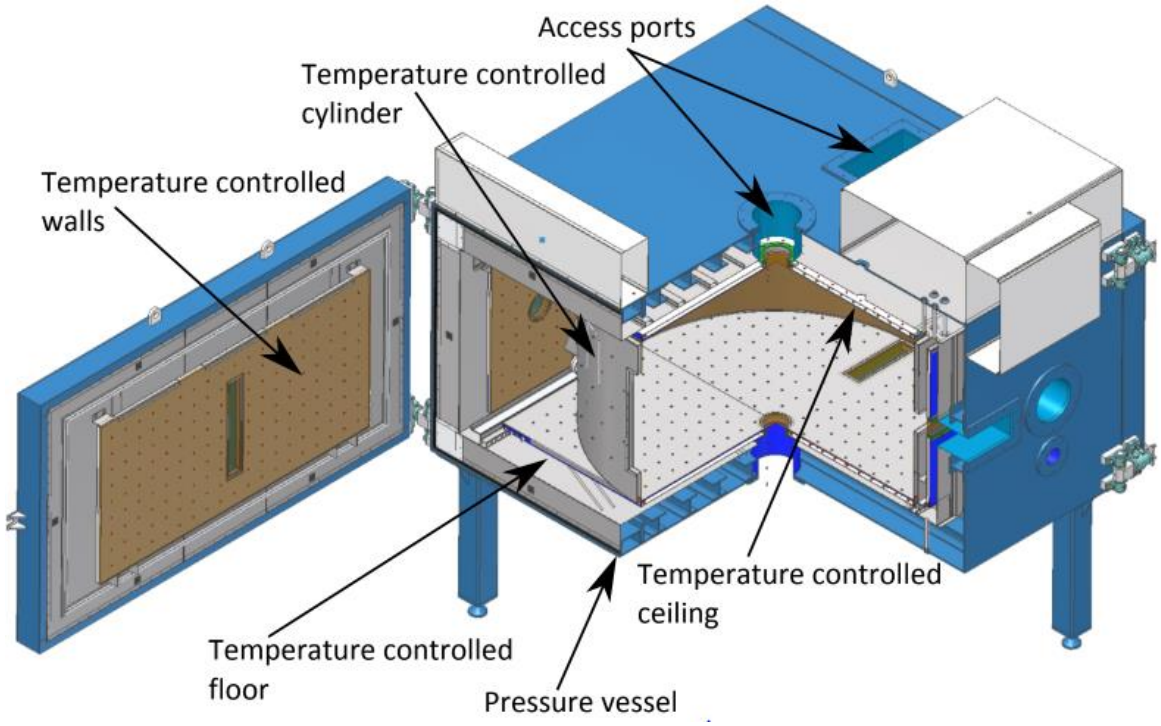

Figure 2. Model of Pi Chamber at MTU. In this sketch, the side door is open, and the cylindrical panel is in place. As can be seen, the walls, ceiling and floor are set-up for temperature and pressure control. Moisture is added by saturating a mesh cloth on the floor. Access ports allow for cloud nuclei to be added. (Chang, 2016)

For the experiments performed in the Pi chamber in summer of 2022 and used in this thesis, resistance temperature detectors (RTDs) and a sonic anemometer were positioned at mid-height throughout the chamber. There were eight RTDs which were spaced throughout the chamber close to the wall in order to monitor the large scale flow of the chamber. The sonic anemometer was placed directly under the thermistor array so as to measure the speed of the air coming down onto the thermistor array. Figure 4 shows a diagram of the set-up of the Pi Chamber. The RTDs are on the horizontal midplane of the chamber and are spaced with π/4

radians between each one and its neighbors. The RTDs used were 100 **Ω**, thin-film, platinum-resistance thermometers (Minco, S17624, 100 **Ω** ± 0.12 %).

The thermistors used (see figure 3) were dissipation constant in still air within a time frame of 0.5 seconds. Their nominal resistance at 25° F to 77° F was 2,000**Ω** to 8,000**Ω**. Their termination material was glass to metal header. The thermistors consisted of two beads, each bead being mounted to a special hermetically-sealed header and having a 75mm lead length. (Honeywell, S115)

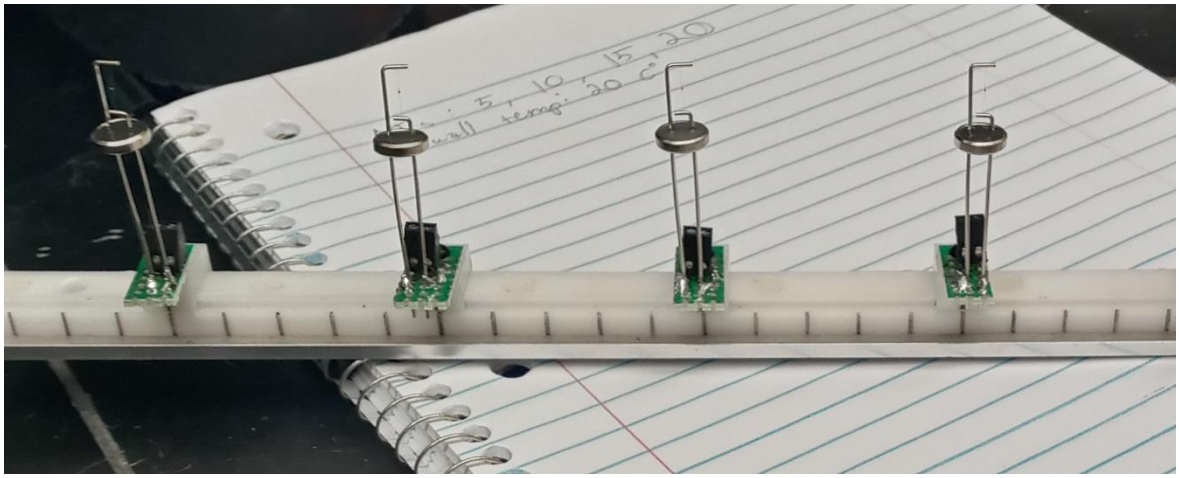

Figure 3. Close up of thermistors used. Their termination material was glass to metal header. The beads were mounted to a special hermetically-sealed header and had a 75mm lead length. (Honeywell, S115)

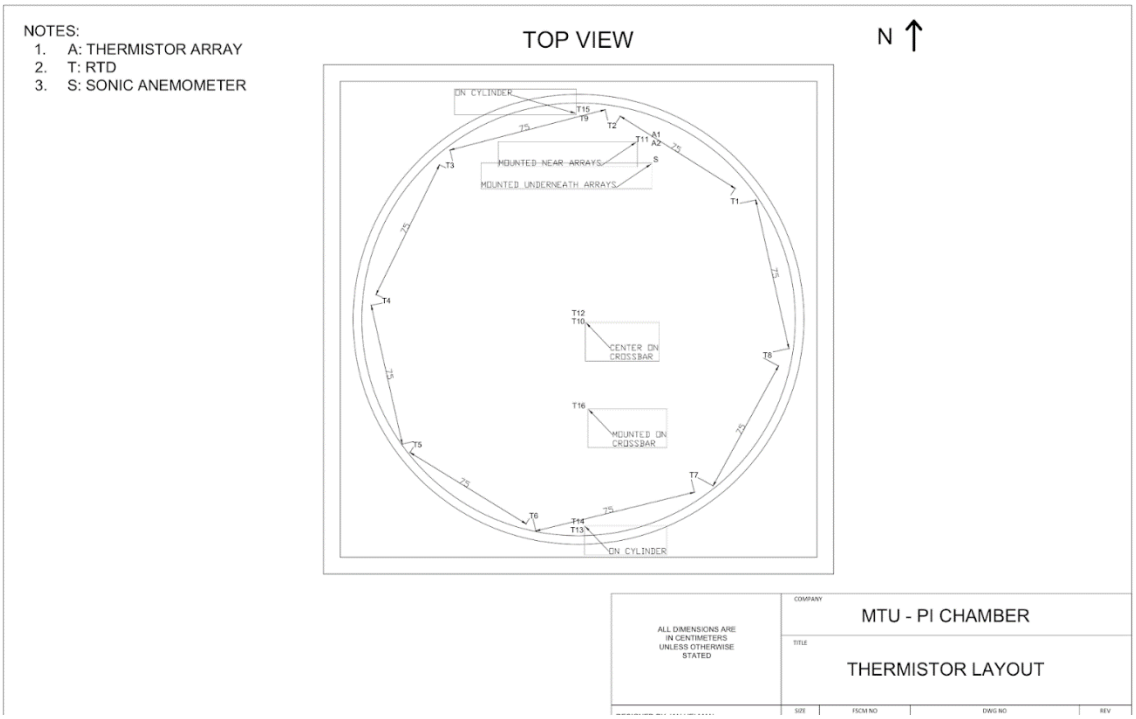

Figure 4. Top view diagram of Pi Chamber. Eight RTDs are positioned at mid height along the walls of the chamber. The thermistor array and sonic anemometer are positioned along the wall close to the downdraft. (Provided by Ian Helman at Michigan Tech)

The thermistor array is built from ten thermistors as shown in figure 5 (a). They were set up in two rows. The first row had thermistors 1 through 7. The second row had thermistors 8 through 10. The distance between the thermistors within the row (between 1 and 2, or 8 and 9), is referred to as δx. The distance between the two rows (between 3 and 8, or 5 and 10) is δy. The thermistors were wired to adjustable bread boards so their position along the array could be changed. This made δx adjustable. δy was held constant at ~6cm (see figure 5).

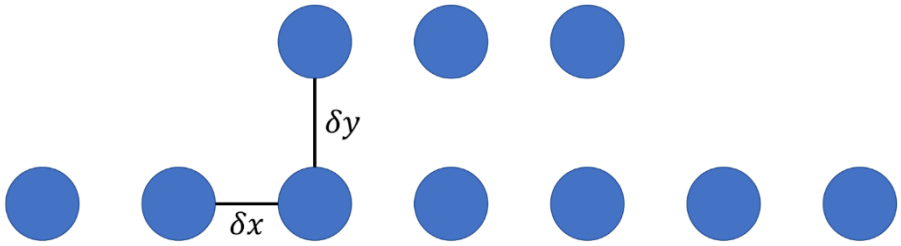

(a)

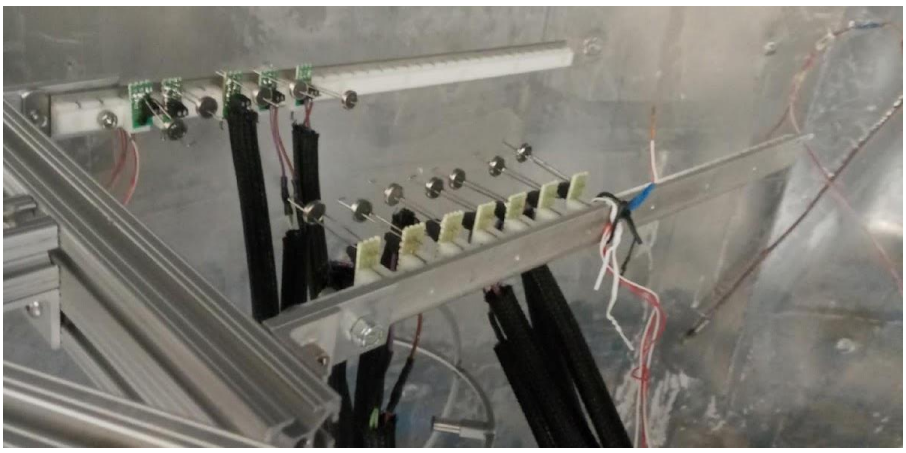

(b)

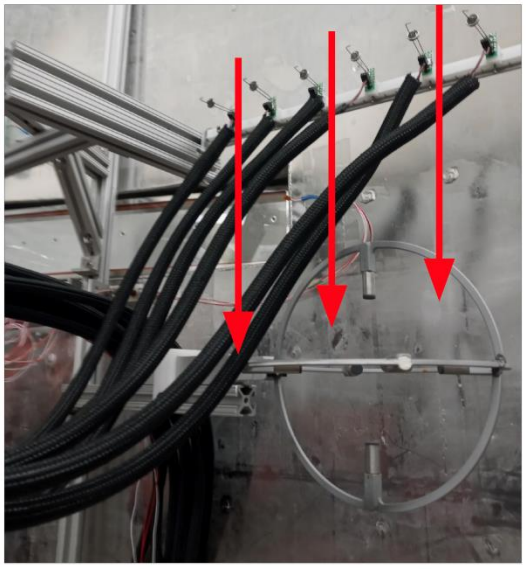

(c)

Figure 5. a) diagram of thermistor array. b) Photo of thermistors mounted in the Pi Chamber. c) Photo of thermistor array mounted with the sonic anemometer; downdraft depicted.

2.2: Turbulence in the Chamber

The turbulent flow within the Pi Chamber is induced by the difference in temperature between the floor and the ceiling. The air close to the floor is warmed and so begins to rise. The ceiling is kept at a cooler temperature than the floor. When the air reaches the ceiling, it cools and so begins to sink. This constant upward and downward motion creates Rayleigh-Benard turbulence.

The turbulence created is made up of eddies of varying sizes, including an eddy roughly the size of the Pi Chamber. This is the dominant circulation in the Pi Chamber. It can be monitored using the RTDs and thermistor array.

The thermistor array was attached to a harness which sat close to the wall above the sonic anemometer. The thermistors pointed towards each other facing the ceiling in the portion of the large eddy down-draft (see figure 5 (c)). This was done to diminish the effects of instrumentation on the turbulence being measured.

2.3: Large Scale Circulation of the Pi Chamber

In order to determine the direction of the large scale circulation (LSC) within the Pi Chamber, histograms of the data taken were plotted. Although the temperature of the Pi Chamber averages to 20°C, the ceiling is cooler, and the floor is warmer. Because this experiment is focusing on the turbulent fluctuations, we are less concerned with the mean temperature and more with the changing in temperature.

However, this information can be used to determine the LSC. Because of this, if the thermistor array is located in an updraft, the average air temperature will be slightly cooler than 20°C and the histogram will be positively skewed. If it is located in a downdraft, the average air temperature will be slightly warmer than 20°C and the histogram will be negatively skewed.

To find the LSC, a histogram is taken of the data. If the histogram is positively skewed, the thermistors are in an updraft. However, if the histogram is negatively skewed, the array is in a downdraft, which gives cleaner data. This method is similar to the method used in Anderson et al. (2021). It is important that the thermistor array be close to the downdraft to ensure the purest representation of thermal turbulence. This downdraft will be used as the mean wind later on in the use of Taylor's Frozen Turbulence Hypothesis.

Figure 6 shows the raw data histogram for thermistor 5 of various runs. Most histograms showed a negative skew which is consistent with the thermistors being in the downdraft. However, it was noticed that the histogram plots of the data taken on the 8th showed the LSC changing directions for an hour or two. Figure 6 subplot (e) shows the LSC changing directions during the 15K run. Due to this, more 3.5cm spaced data was taken later. The 15K run for the 3.5cm data was replaced with the newer data. The newer data's histogram is shown in subplots (g) and (h).

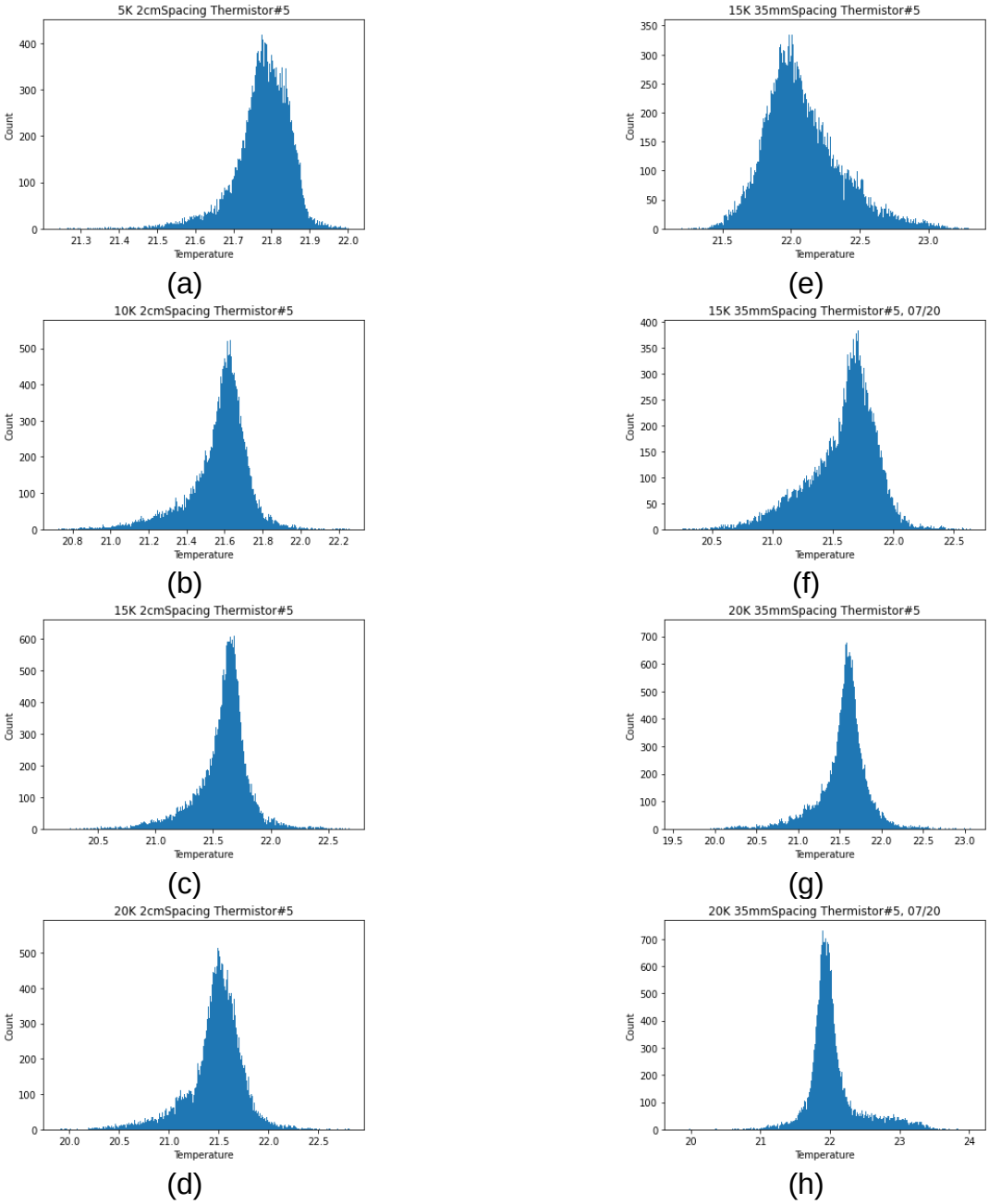

Figure 6. Raw data histograms for thermistor 5 of various runs. Shown are 5K (a), 10K (b), 15K (c) and 20K (d) for 2 cm spacing. Also shown are 15K (e,f) and 20K (g,h) for 3.5 cm spacing taken two different days.

2.4: Experimentation

For the experiment, the Pi chamber was then closed and ran for twelve hours. During this time, the difference in temperature was stepped up every two hours. The difference in temperature between the floor and the ceiling were 20k, 15k, 10k and 5k, with the average of the floor and the ceiling remaining at 20°C.

The temperature was monitored. When it stabilized, the thermistor array gathered data for an hour. After the data was gathered, the temperature was changed to the next step. This continued for all four temperature steps. This experiment was repeated three times: δx = 2cm, δx = 3.5cm, δx = 5cm. δy remained at ~6cm.

Figure 7 shows a sample of the raw data collected. The thermistors are calibrated to measure temperature fluctuations, but not an accurate mean temperature. As seen in the data, the thermistors are biased from each other. This is not important with the calculations being done in this research as the average will be subtracted out. The LSC periodicity can be seen in Figure 7. There is a slight periodicity to the overall highs and lows which is caused by the Pi Chamber's LSC.

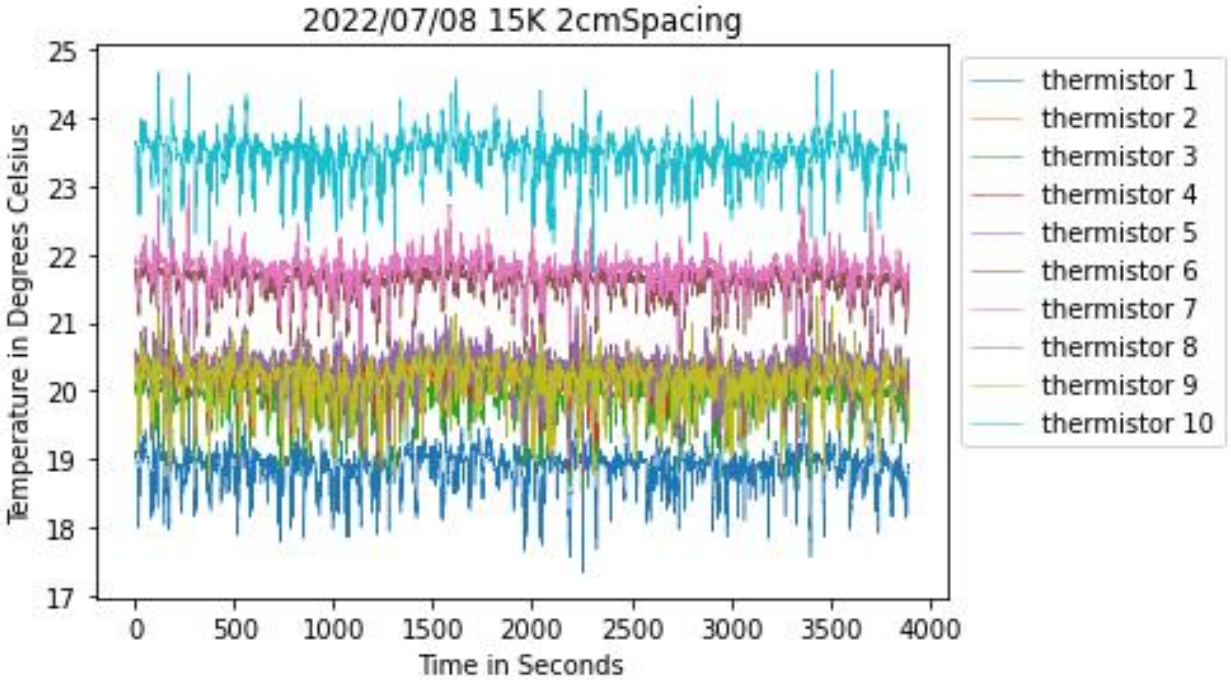

(a)

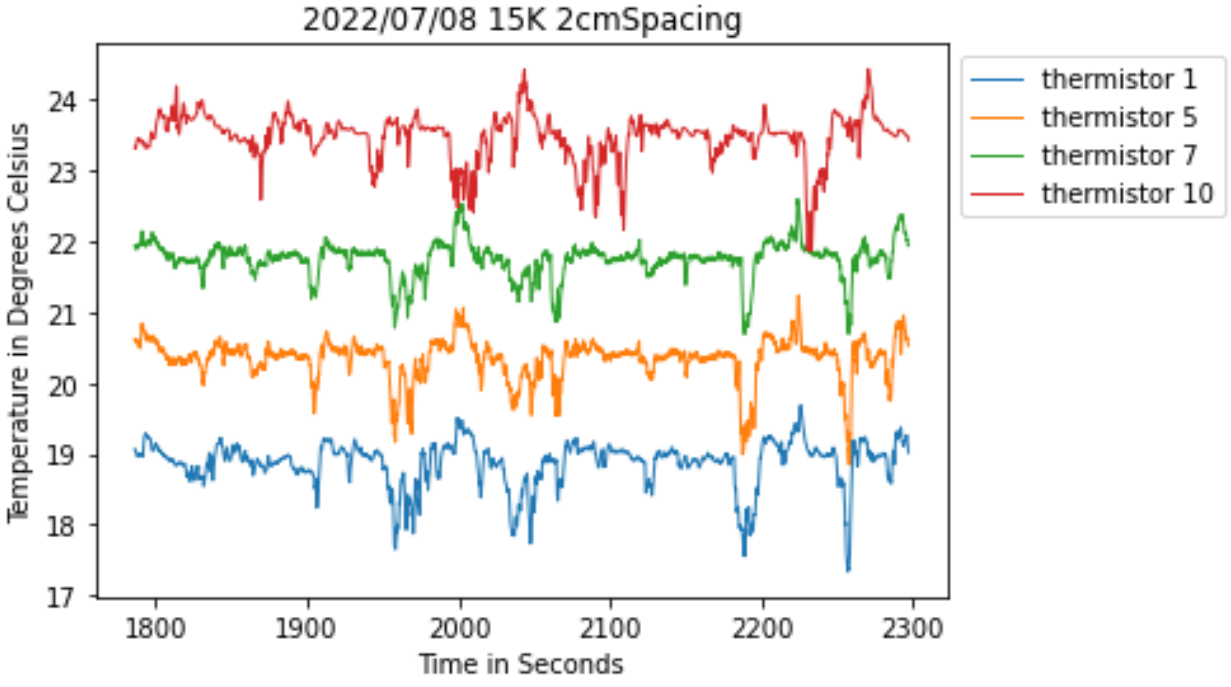

(b)

Figure 7. Raw thermistor data. Figure (a) shows the raw data for the entire hour-long run for all ten thermistors. Figure (b) is approximately ten minutes of data from only four thermistors.

2.5: Filtering for Models

After the data was collected, the Fast Fourier Transform was used to convert it into frequency space. Once the data was in frequency space, it was filtered and then converted back into time space. This imitates how the same data would look with a larger grid-spacing. The data was then split into the data which was not filtered out and the data which was filtered out which imitates the grid-scale turbulence and the subgrid-scale turbulence (see figure 1). The subgrid-scale turbulence was what was used in a priori analyses to finish crafting the subgrid-scale turbulence models.

Two filters were used in this experiment, the box filter and the Gaussian filter (Pope, 2000). The box filter takes pockets of turbulence and effectively smooths them out (equation 6). Though the turbulence is cut-off sharply in physical space, it adds a slight oscillation to the turbulence data in wavenumber space. Often, this slight oscillation is inconsequential. In an effort to eliminate the oscillatory effects of the box filter in wavenumber space, the sharp spectral filter gives a sharp cut-off in wavenumber space (equation 7). Turbulence is not averaged in the same way in physical space. The Gaussian filter filters the data in wavenumber space through a Gaussian curve (equation 8). Unlike previous filters, there is not a dramatic suppression of high-wavenumber components, but rather a gradual cut-off.

$$\hat{G}(k) = \frac{\sin\left(\frac{1}{2}\kappa\Delta\right)}{\frac{1}{2}\kappa\Delta} \quad \text{(equation 6)}$$

$$\hat{G}(k) = H(\kappa_c - |\kappa|) \quad \text{(equation 7)}$$

$$\hat{G}(k) = \exp\left(-\frac{\kappa^2\Delta^2}{24}\right) \quad \text{(equation 8)}$$

It can be useful when there is an interest in both wavenumber space and physical space. Figure 8 shows the data in physical space and wavenumber space for unfiltered, box-filter, sharp-spectral-filter and the gaussian-filter.

The filters filter frequencies of roughly 20 Hz and greater. The effects of the filters can be seen on the graphs on the right. The sharp spectral filter cuts out all filtered frequencies. On the left, it can be seen that the filter has averaged out the data, making it less extreme. The box filter diminishes the highest points in the data in physical space, but has little other effect. In wavenumber space, the oscillation caused by the box filter can be clearly seen in the frequencies after 20Hz. The effects of the Gaussian filter in physical space is very similar to the box filter. The difference can be seen in wavenumber space. Similar to the sharp spectral filter, the Gaussian filter eliminates the higher frequencies. However, it does so gradually rather than with a sharp cut.

For the data which was collected summer of 2022, the turbulence in physical space was of more interest than the turbulence in spectral space. Because of this, only the box filter and Gaussian filter will be used for the research done in this thesis.

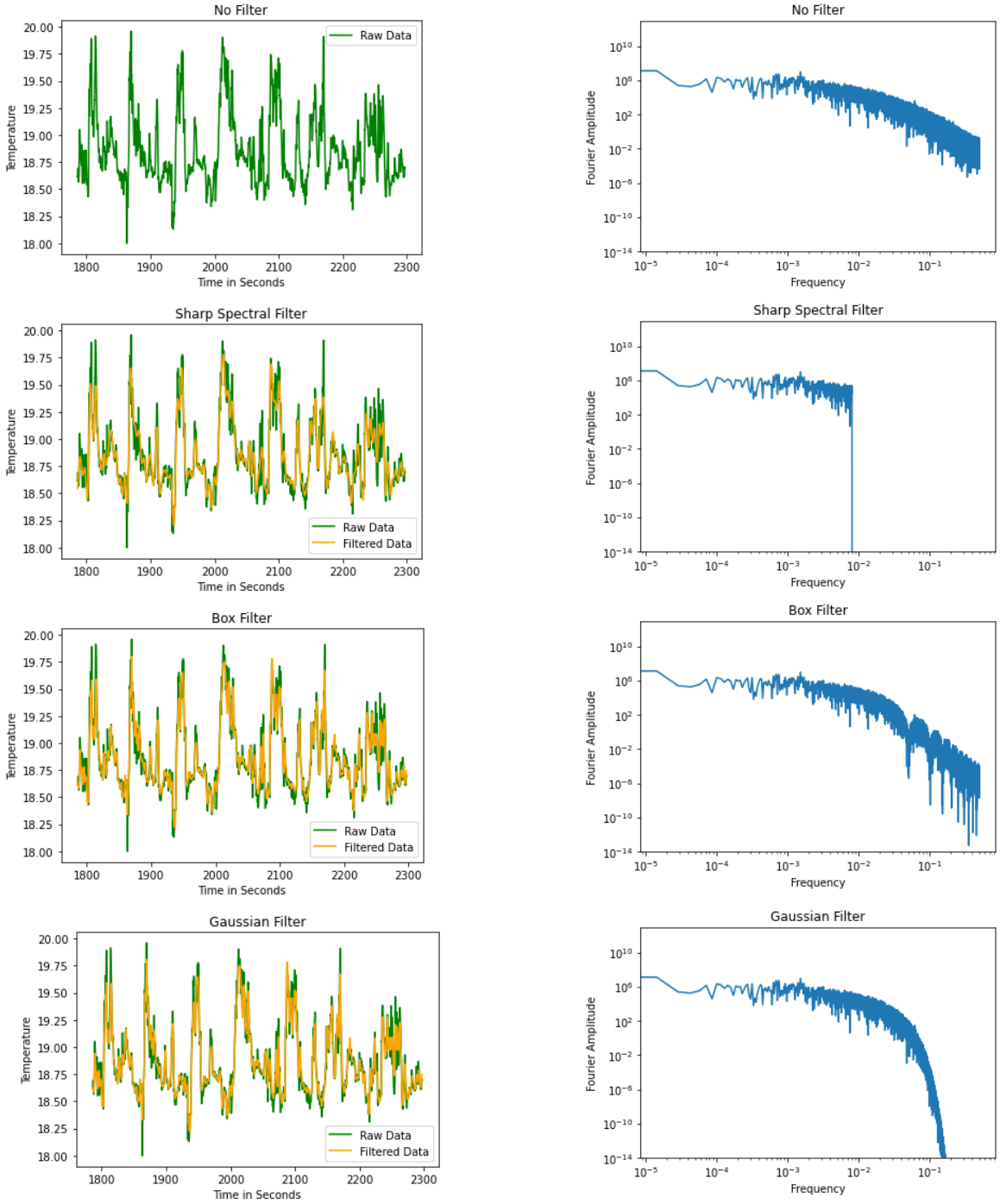

Figure 8. Data in physical space and frequency space for no filter and all three filters. Data shown is from the 15K 3.5cm run on 07 Jul, 2022. Data in physical space is zoomed up on for clarity.

Chapter 3

Results

3.1: Subgrid Scale Temperature Variance

Using both the box-filter and Gaussian-filter filtering systems, the data is filtered in frequency space. This filtered data is then averaged for every time step over three thermistors (see figure 9). This filtered data is referred to in equations as $\tilde{\theta}$. The raw data is also squared before being filtered, which gives $\widetilde{\theta\theta}$. The difference between the squared data filtered and the filtered data squared, is $\tau_{calculated}$ (equation 9).

$$\tau_{calculated} = \widetilde{\theta\theta} - \tilde{\theta}^2 \qquad \text{(equation 9)}$$

τ is the subgrid variance of the data, also referred to as the scalar unmixedness. It measures the degree of local homogeneity of the turbulence (Sagaut, 2001).

After τ is calculated, it is used to find the model coefficients for the two models of interest. The model coefficient is found by averaging $\tau_{calculated}$ over time and dividing it by the time-average of the unscaled model (see equations 11 and 13). A different model coefficient is found for every spatial width and temperature difference. A table of all the model coefficients can be seen in table 1.

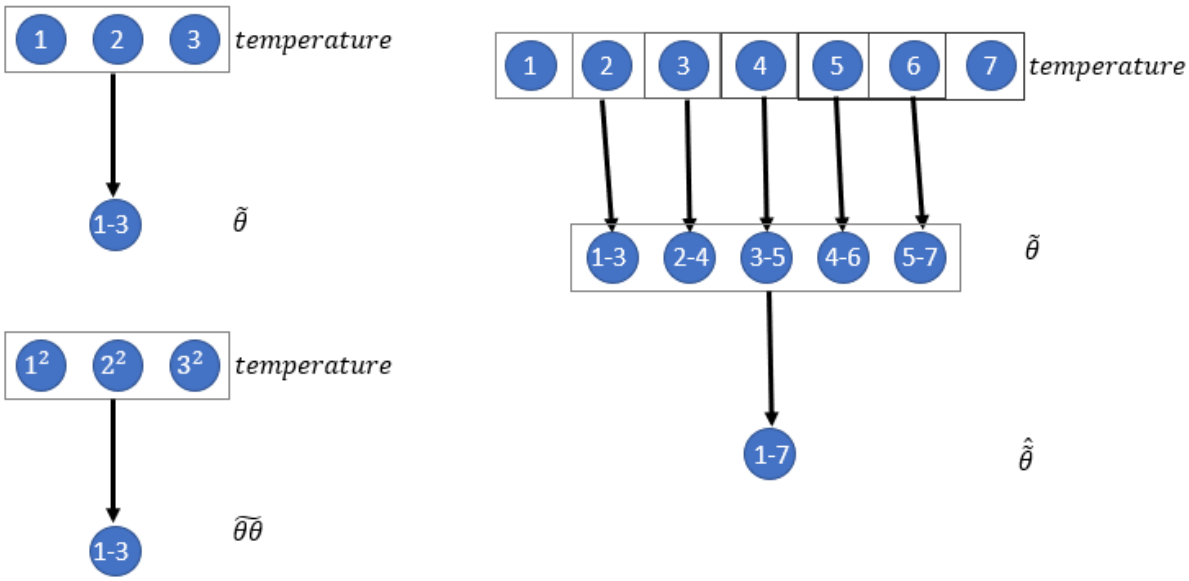

Figure 9. Representation of filtering to get $\tilde{\theta}$, $\widetilde{\theta\theta}$ and $\hat{\tilde{\theta}}$. $\tilde{\theta}$ is the filtered data of three thermistors. $\widetilde{\theta\theta}$ is the average of three thermistors' data after being squared, filtered and then averaged. $\hat{\tilde{\theta}}$ is five $\tilde{\theta}$ filtered.

After the model coefficient is found, it is multiplied by the unscaled model to make the final model. How well this model does can be seen by comparing it to $\tau_{calculated}$ on a point-by-point analysis. The models were analyzed by the use of joint histograms and finding the correlation coefficients for each model and its corresponding calculated τ. These joint histograms can be seen in figures 19-26. A table of the correlation coefficients between $\tau_{calculated}$ and the models is shown in table 2 and figure 27.

3.2: Models Being Studied

Generally, the models made for LES are based on knowledge of fluid mechanics and small-scale turbulence. However, there are variables and coefficients in the models which

remain unknown. To build and better understand these models, data from the Pi chamber experiments will be used to find these unknown coefficients. First, the subgrid-scale data is filtered and compared to the model. Through this comparison, it can be found mathematically the best values for the model coefficients. The models were then compared to $\tau_{calculated}$ (see equation 11 and equation 13) to determine how well the model works. The ways to compare the models with $\tau_{calculated}$ include histograms, joint histograms and correlation coefficients.

In this paper, a different model coefficient is found for every horizontal spacing and every temperature step. Table 1 shows what these coefficients are.

3.2.1 Scale-Similarity Model

The first model of interest is the scale-similarity model (see equation 10). A scale-similarity type model can be obtained by using the zeroth-order expansion of the deconvolution operator (Sagaut, 2001).

$$\tau_{calculated} = C_{sim}(\widehat{(\tilde{\theta}^2)} - (\hat{\tilde{\theta}})^2) \qquad \text{(equation 10)}$$

In equation 10, $\hat{\tilde{\theta}}$ represents the filtering of five $\tilde{\theta}$s. Because each $\tilde{\theta}$ is the filtering of three thermistors, seven thermistors are necessary to calculate a single value for $\hat{\tilde{\theta}}$ (see figure 9). In this paper, C_{sim} will be calculated via equation 11. Table 1 and figure 10 show the values calculated for C for both the box-filter and the Gaussian-filter.

$$\frac{\langle \tau_{calculated} \rangle}{\left\langle \left(\widetilde{(\tilde{\theta}^2)} - \left(\hat{\tilde{\theta}} \right)^2 \right) \right\rangle} = C_{sim} \qquad \text{(equation 11)}$$

In the equation shown above, $\tilde{\theta}$ and $\hat{\tilde{\theta}}$ were found using the method shown in figure 9. $\tau_{calculated}$ was found using equation 9 and then averaged over time. The model shown in equation 10 was calculated and then also averaged over time. Averaging them both and then dividing $\tau_{calculated}$ by the unscaled model gives the average over time of C_{sim} from equation 11. This average C_{sim} will be used for every point in time for the same spacing and temperature difference.

3.2.2 Gradient Model

The other model being investigated is the Gradient model. In 1991, Germano et al. proposed a model which would come to be known as the Germano model. At the time, he argued that models of subgrid-scale eddy viscosity up to that point were unable to represent correctly with a single universal constant for different turbulent fields. This included fields in rotating or sheared flows, near solid walls, or in transitional regimes. Germano's model was an attempt to fix these drawbacks. The model is based on an algebraic identity between the subgrid-scale stresses at two different filtered levels and the resolved turbulent stresses.

Mostly, the identity has been applied to closures for the subgrid-scale fluxes required in large eddy simulations in the bulk of turbulent flows. However, the basic ideas underlying the Germano identity can be applied in various other contexts. These various applications are explored by Meneveau, 2012. One application is the building of the Gradient model

used in this paper. This model is found using a dynamic procedure based on a Germano-type identity (Meneveau, 2012). Equation 12 shows the model used.

$$\tau_{calculated} = C_{grad}\left(\widehat{\Delta}\right)^2 \left|\nabla\hat{\tilde{\theta}}\right|^2 \qquad \text{(equation 12)}$$

For this model, C_{grad} will be calculated via equation 13.

$$\frac{\langle\tau_{calculated}\rangle}{\left\langle\left(\widehat{\Delta}\right)^2\left|\nabla\hat{\tilde{\theta}}\right|^2\right\rangle} = C_{grad} \qquad \text{(equation 13)}$$

In this equation, $\hat{\tilde{\theta}}$ was found using the method shown in figure 9. ∇ denotes the gradient of $\hat{\tilde{\theta}}$. The derivative in the x direction was found by comparing data from various thermistors within the same array. The derivative in the y direction was found by comparing the data from thermistors in the two arrays; because the derivative was being found for $\hat{\tilde{\theta}}$, three thermistors were needed in the second array for this calculation. The derivative in the z direction was found using Taylor's Frozen Turbulence Hypothesis; the speed of the turbulence was found using the sonic anemometer allowing for the derivative in the z direction to be found for each thermistor individually by comparing earlier readings to later readings (Schlipf, 2011). $\tau_{calculated}$ was found using equation 9 and then averaged over time. The model shown in equation 12 was calculated and then also averaged over time. The C_{grad} calculated in equation 13 was used for every point for the same spacing and temperature difference.

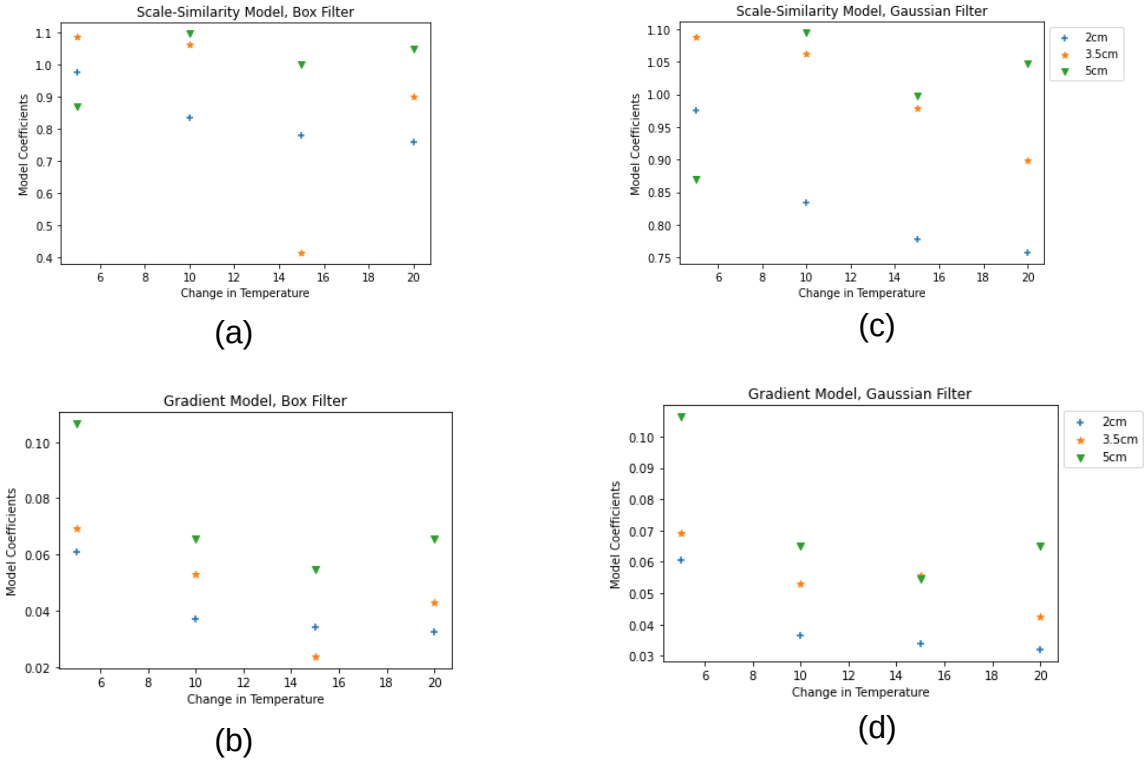

Figure 10. Model coefficients versus difference in temperature between the floor and the ceiling. Figures shown are of the Scale-Similarity Model and Gradient Model for all three spacings for box filter (a-b) and Gaussian filter(c-d).

In both equation 11 and equation 13, a single value of C is found for every temperature step and change in distance spacing. The values for these model coefficients are shown in table 1 and figure 10.

These coefficients were then inserted back into equations 10 and equation 12. The calculated models were then compared to the original $\tau_{calculated}$ calculated by equation 9. Histograms and joint histograms comparing the models to $\tau_{calculated}$ are

shown in figures 11-26. A correlation coefficient was calculated for $\tau_{calculated}$ and the scaled models. These values are shown in table 2 and figures 19-27.

Figures 11-18 show the normalized histograms of modeled τ and $\tau_{calculated}$ for both the scale-similarity model and the gradient model. On the left are the full histograms. On the right are the histograms zoomed up on the peaks. The comparison of the histograms helps to demonstrate how well the model represents the gathered data. When the peaks are close together and roughly the same count, this shows that the modeled data is a good representation of the statistics of the gathered data.

Model Coefficients					
		Scale-Similarity Model		Gradient Model	
δx	δ Temperature	Box-Filter	Gaussian- Filter	Box-Filter	Gaussian- Filter
2 cm	5K	0.9736	0.9759	0.06095	0.06063
	10K	0.8347	0.833	0.03697	0.03655
	15K	0.7775	0.7767	0.03429	0.03389
	20K	0.7577	0.7572	0.03248	0.03203
3.5 cm	5K	1.087	1.0874	0.06951	0.06927
	10K	1.063	1.0619	0.05316	0.05284
	15K	0.9806	0.9793	0.05617	0.05569
	20K	0.9	0.8993	0.04287	0.04254
5 cm	5K	0.8693	0.8693	0.1065	0.1063
	10K	1.095	1.0945	0.0655	0.06523
	15K	0.9983	0.9973	0.05474	0.0545
	20K	1.0473	1.0472	0.06534	0.0641

Table 1. Model coefficients for all three spacings, all four temperature gradients, both models and both filters. The model coefficient is a scaling variable between $\tau_{calculated}$ and the models and so has no units.

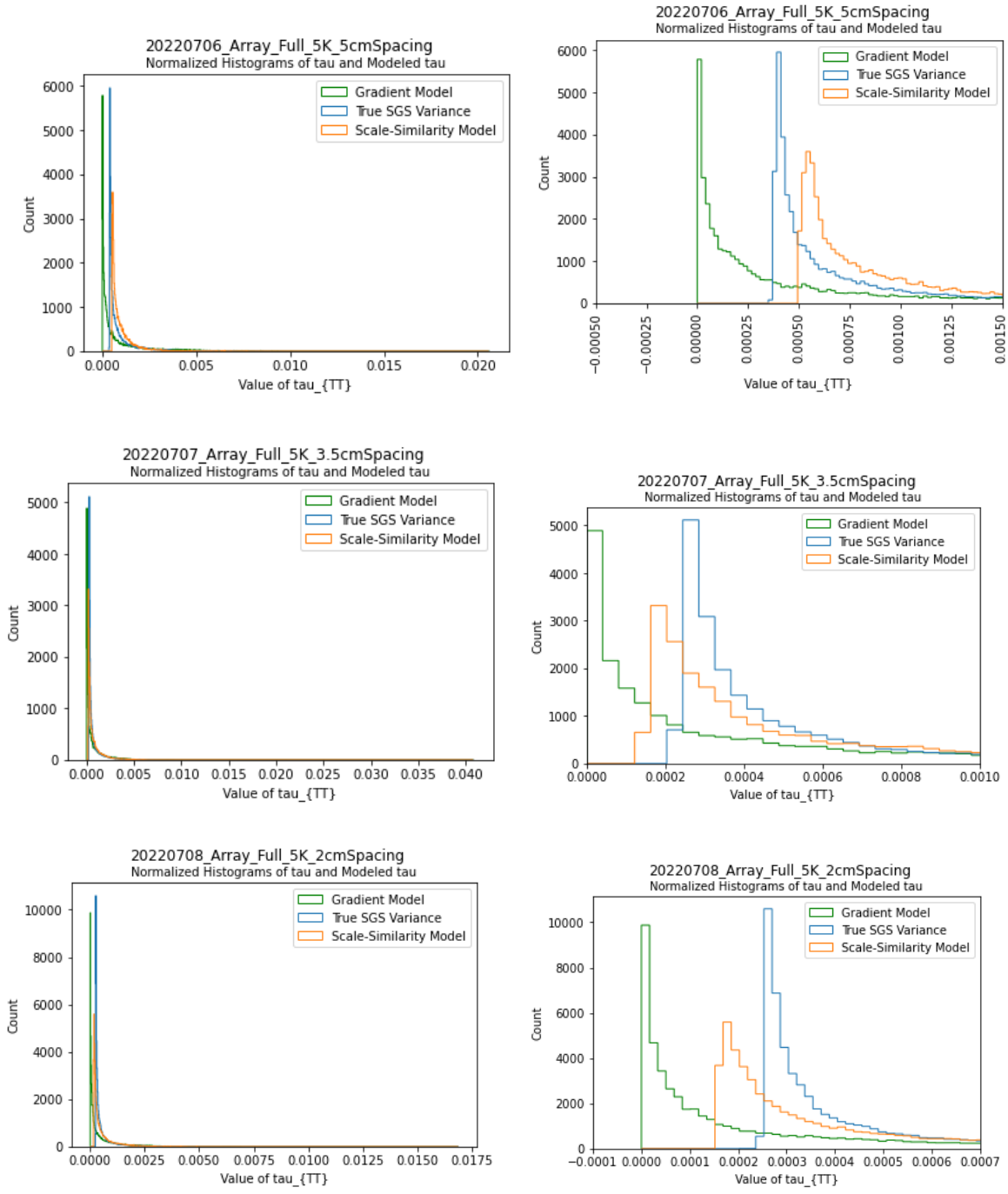

Figure 11. Normalized histogram plots of 5K measurements at three different widths. On the Left is the full plot. On the right is the plot zoomed in at the peak. Gaussian-filter was used for all plots shown.

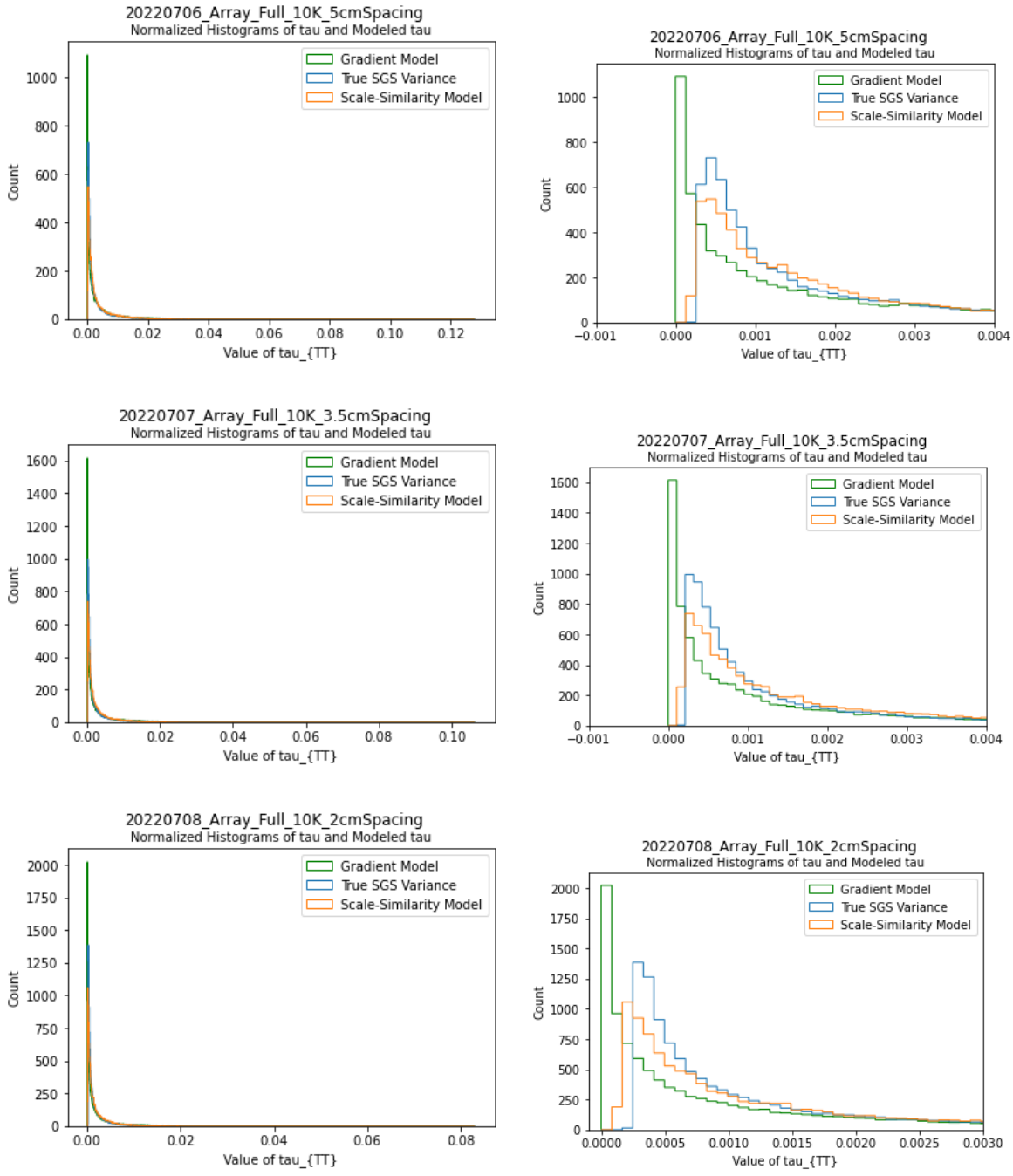

Figure 12. Normalized histogram plots of 10K measurements at three different widths. On the Left is the full plot. On the right is the plot zoomed in at the peak. Gaussian-filter was used for all plots shown.

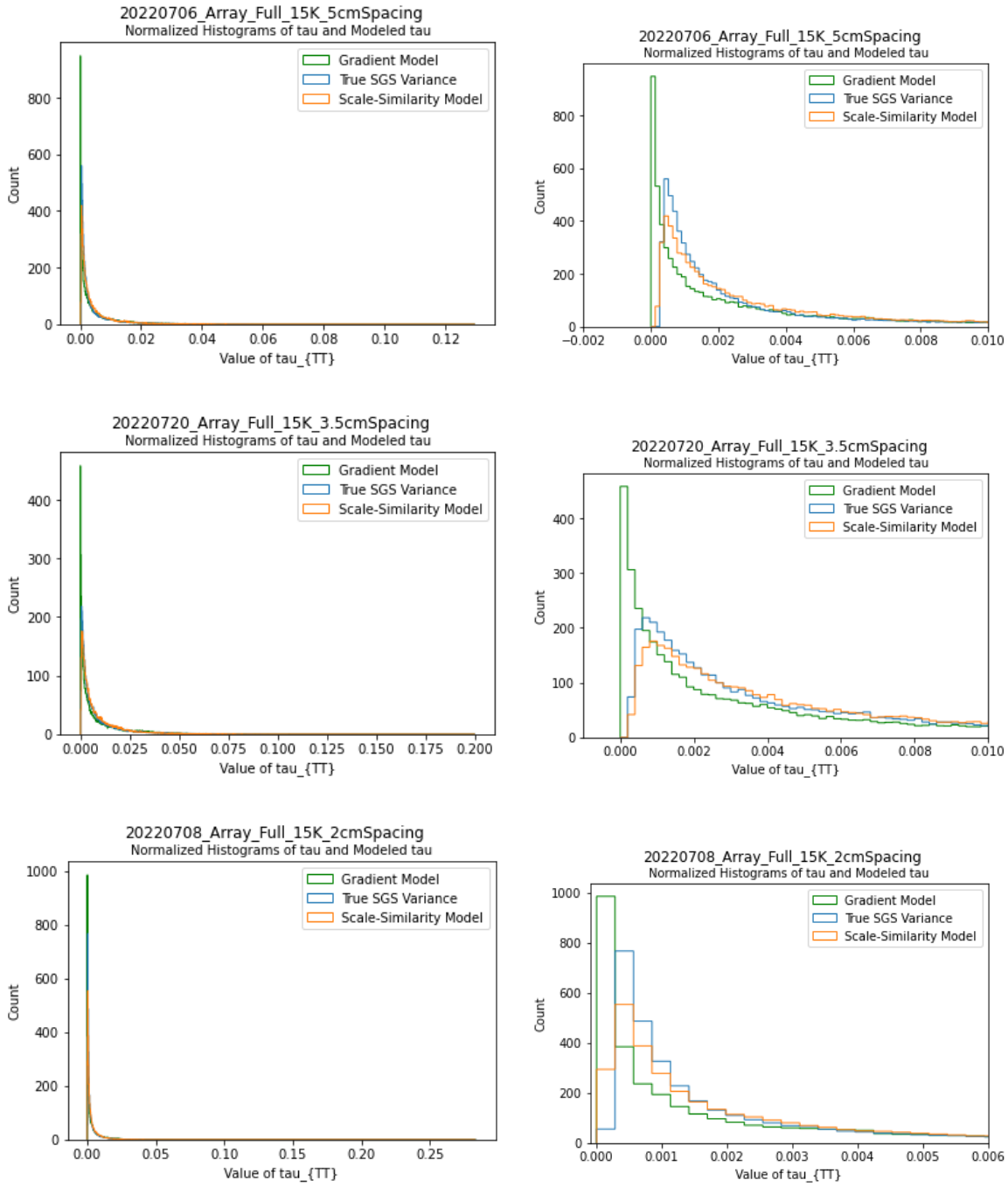

Figure 13. Normalized histogram plots of 15K measurements at three different widths. On the Left is the full plot. On the right is the plot zoomed in at the peak. Gaussian-filter was used for all plots shown. Data taken on the 7th was replaced with data taken on the 20th due to the data taken on the 7th being in the updraft instead of the downdraft.

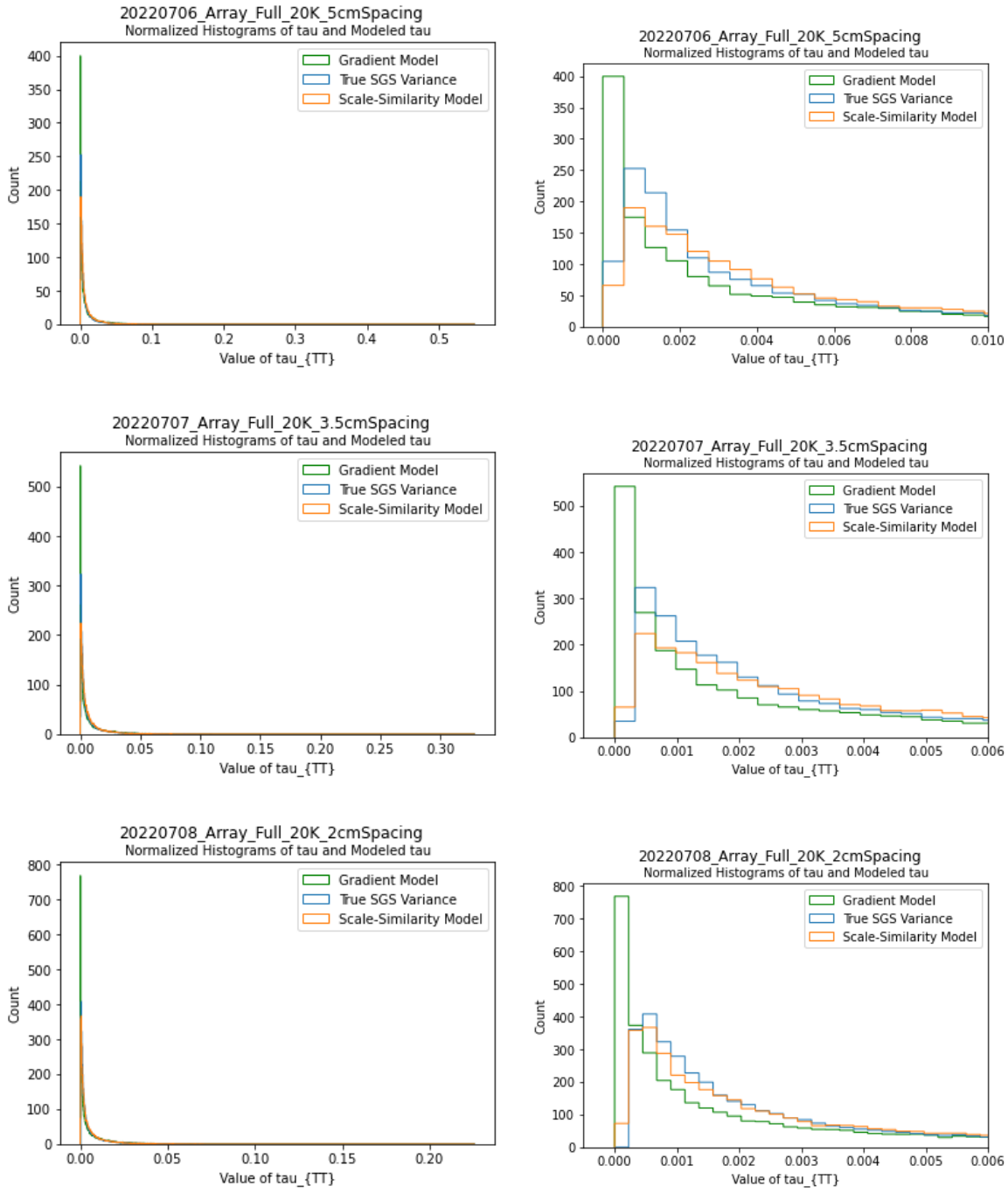

Figure 14. Normalized histogram plots of 20K measurements at three different widths. On the Left is the full plot. On the right is the plot zoomed in at the peak. Gaussian-filter was used for all plots shown.

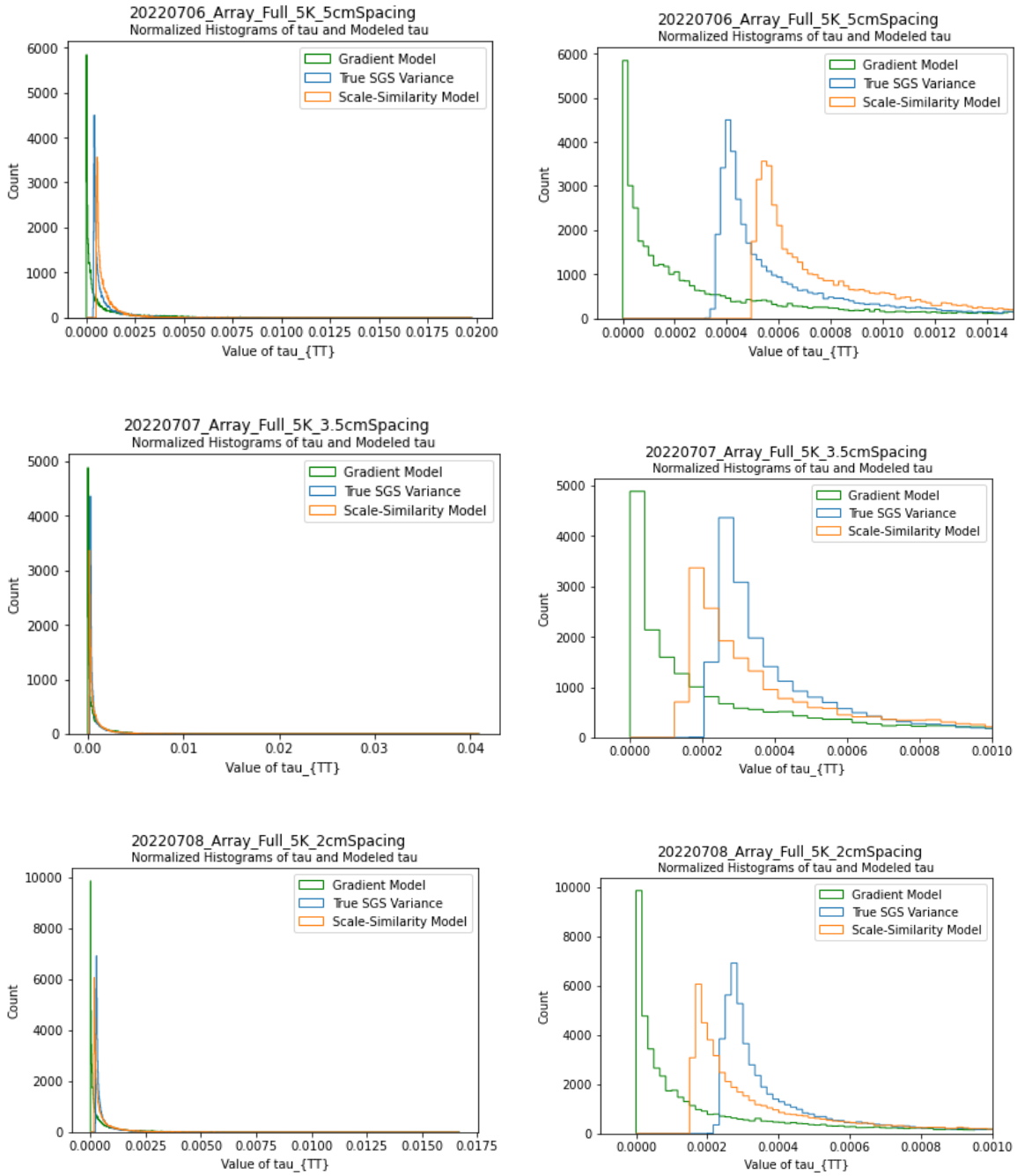

Figure 15. Normalized histogram plots of 5K measurements at three different widths. On the Left is the full plot. On the right is the plot zoomed in at the peak. Box-filter was used for all plots shown.

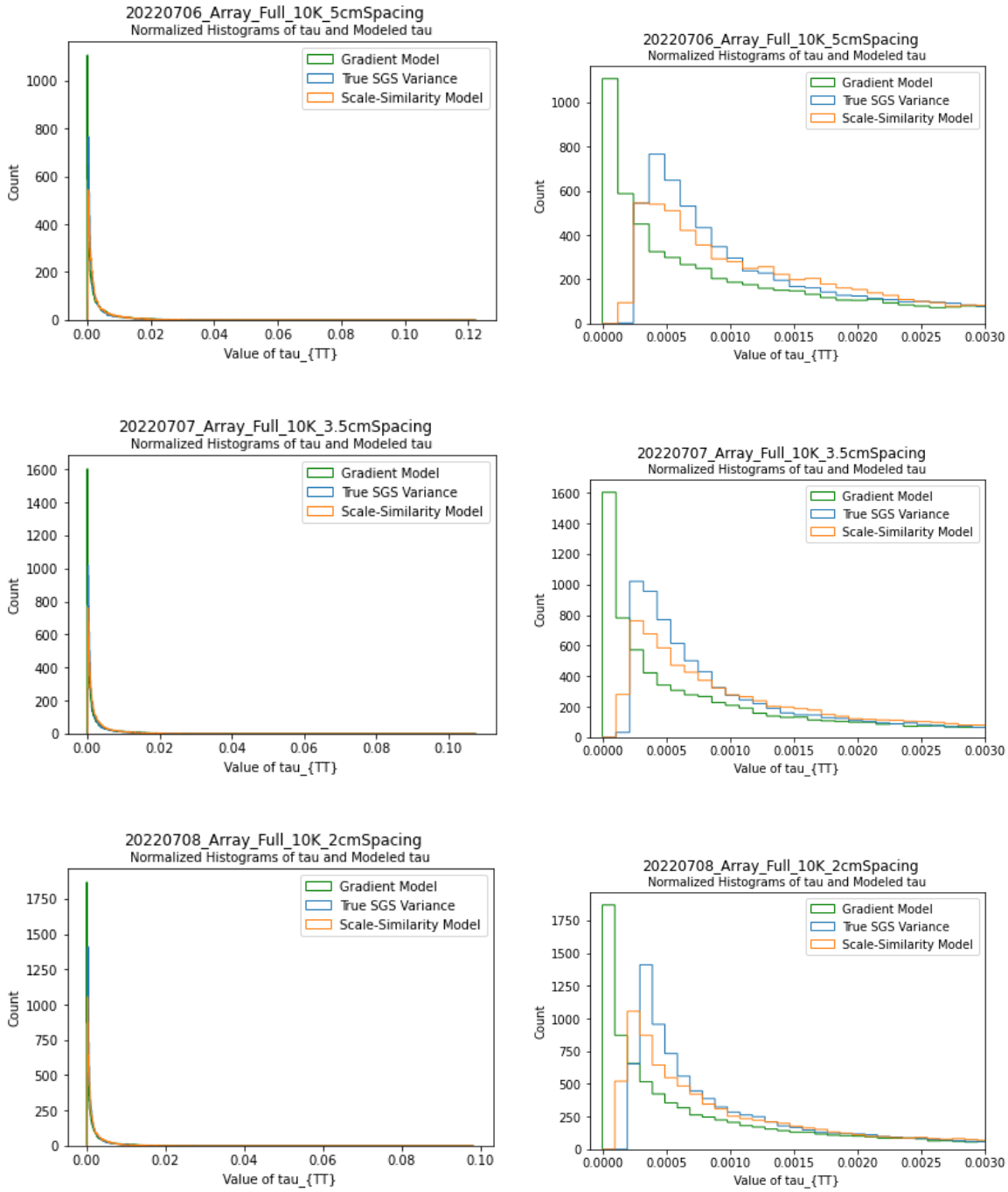

Figure 16. Normalized histogram plots of 10K measurements at three different widths. On the Left is the full plot. On the right is the plot zoomed in at the peak. Box-filter was used for all plots shown.

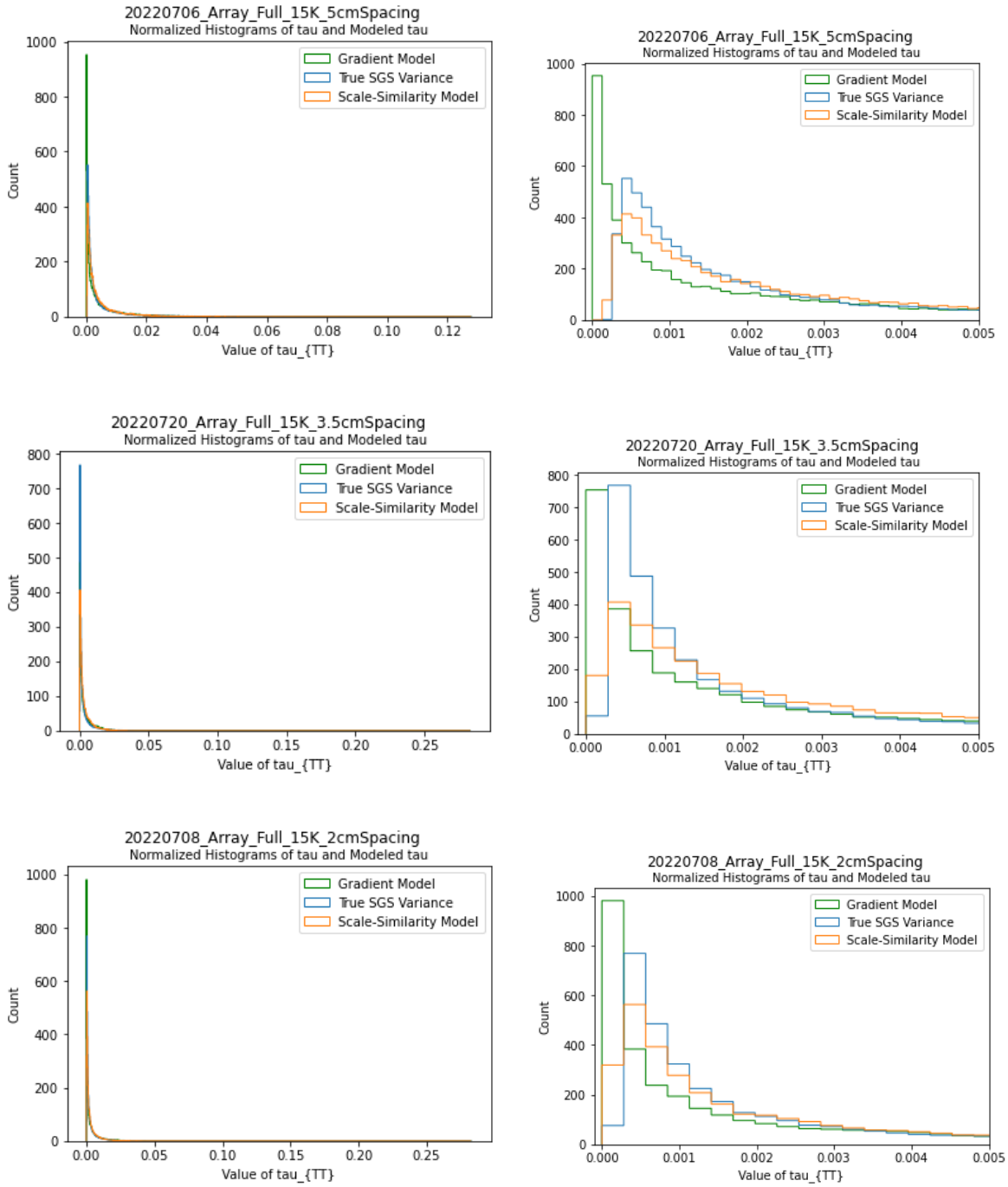

Figure 17. Normalized histogram plots of 15K measurements at three different widths. On the Left is the full plot. On the right is the plot zoomed in at the peak. Box-filter was used for all plots shown. Data taken on the 7th was replaced with data taken on the 20th due to the data taken on the 7th being in the updraft instead of the downdraft.

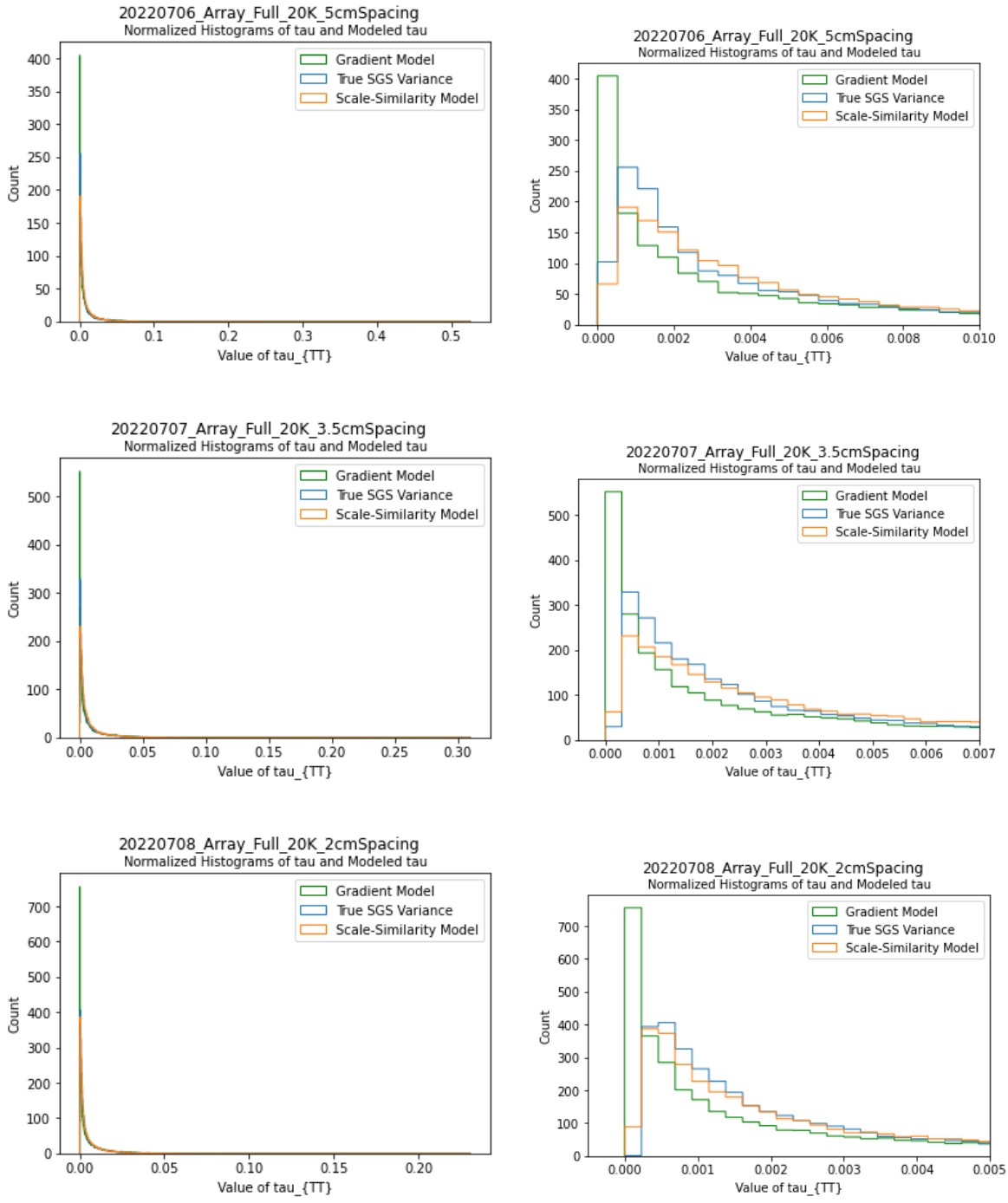

Figure 18. Normalized histogram plots of 20K measurements at three different widths. On the Left is the full plot. On the right is the plot zoomed in at the peak. Box-filter was used for all plots shown.

In the normalized histograms shown in figures 11-18, the Gradient model peaks sooner and higher than the subgrid scale variance. The scale similarity model shows closer resemblance to the true subgrid scale variance, peaking close to the same place and same height. This suggests that the scale similarity model does a better job of modeling the actual variance. However, the Gradient model tends to show lower values than the actual variance. This suggests that the Gradient model under-represents the energy and momentum held in the subgrid scale turbulence.

Joint histograms were also taken of the models and $\tau_{calculated}$ for both the scale-similarity model and the gradient model. Figures 19-26 show the joint histograms. The joint histograms were zoomed in to the corner of greatest interest as determined by the level of correlation. A one-to-one line was plotted on the graphs as well to show how the joint histogram deviates from linear correlation. On most of the graphs it can be seen that the modeled τ has lower values than $\tau_{calculated}$. The scale-similarity model at higher differences in temperature shows a greater degree of linear correlation (compare figures 19 and 23 to figures 22 and 26). For the gradient model, however, τ continues to have much lower values than $\tau_{calculated}$ regardless of the change in temperature. As with the histograms, this suggests that the Gradient model models less energy and momentum in the subgrid scale turbulence than the true subgrid scale turbulence shows.

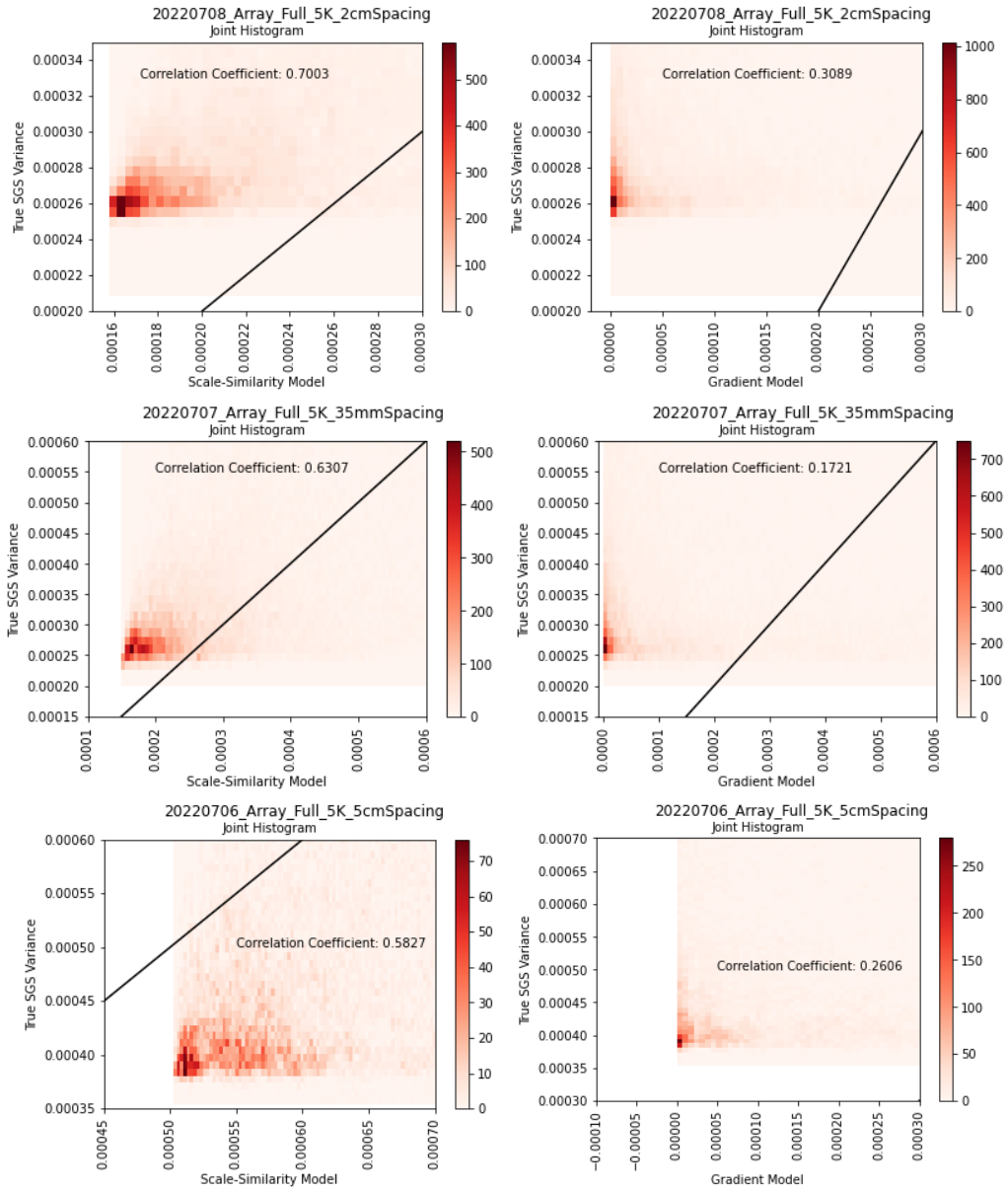

Figure 19. Joint-histogram plots of 5K measurements at three different widths. On the Left is the joint-histogram plot of the calculated variance versus the scale-similarity modeled variance. On the right is the joint-histogram plot of the calculated variance versus the Gradient modeled variance. Gaussian-filter was used for all plots shown.

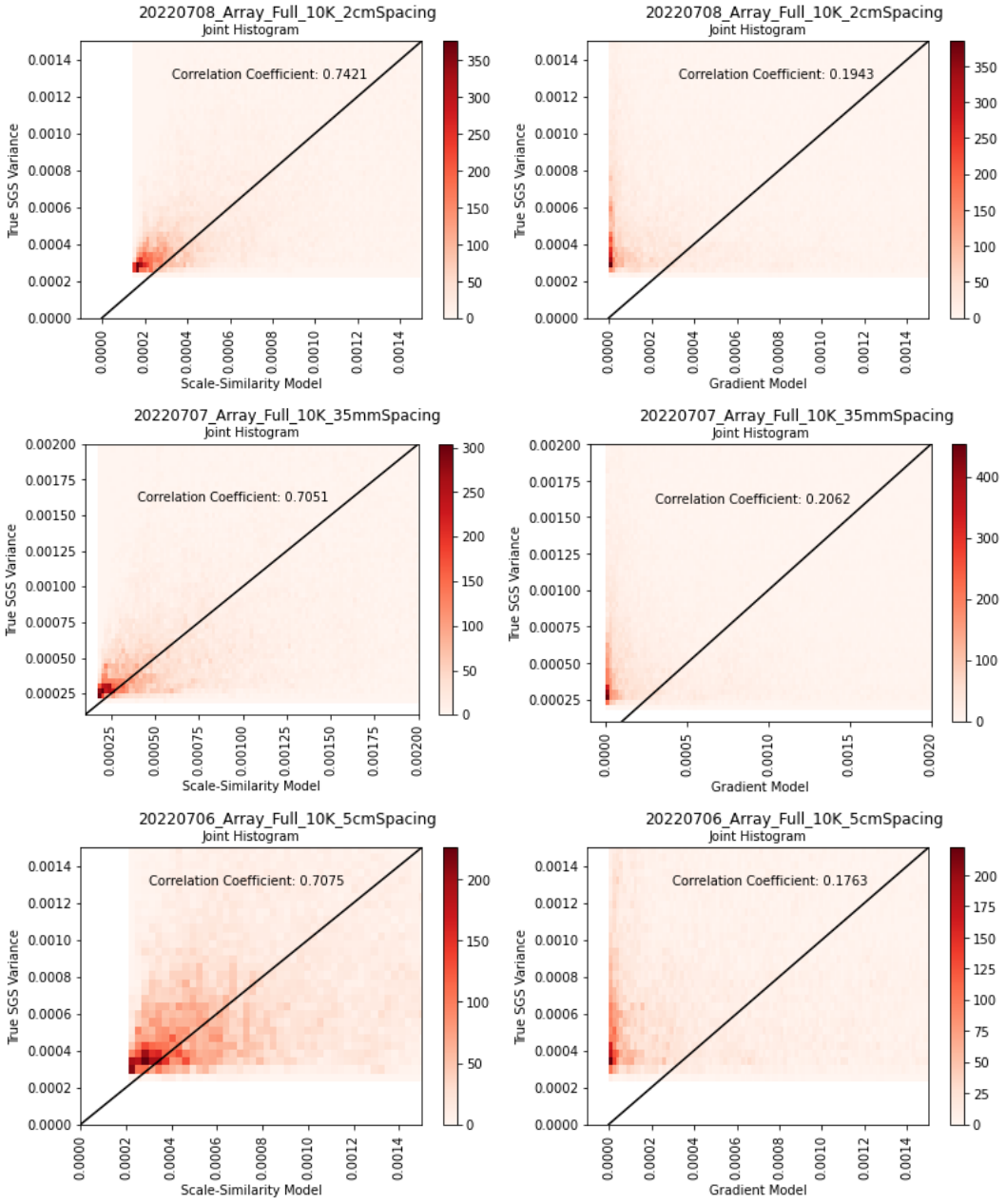

Figure 20. Joint-histogram plots of 10K measurements at three different widths. On the Left is the joint-histogram plot of the calculated variance versus the scale-similarity modeled variance. On the right is the joint-histogram plot of the calculated variance versus the Gradient modeled variance. Gaussian-filter was used for all plots shown.

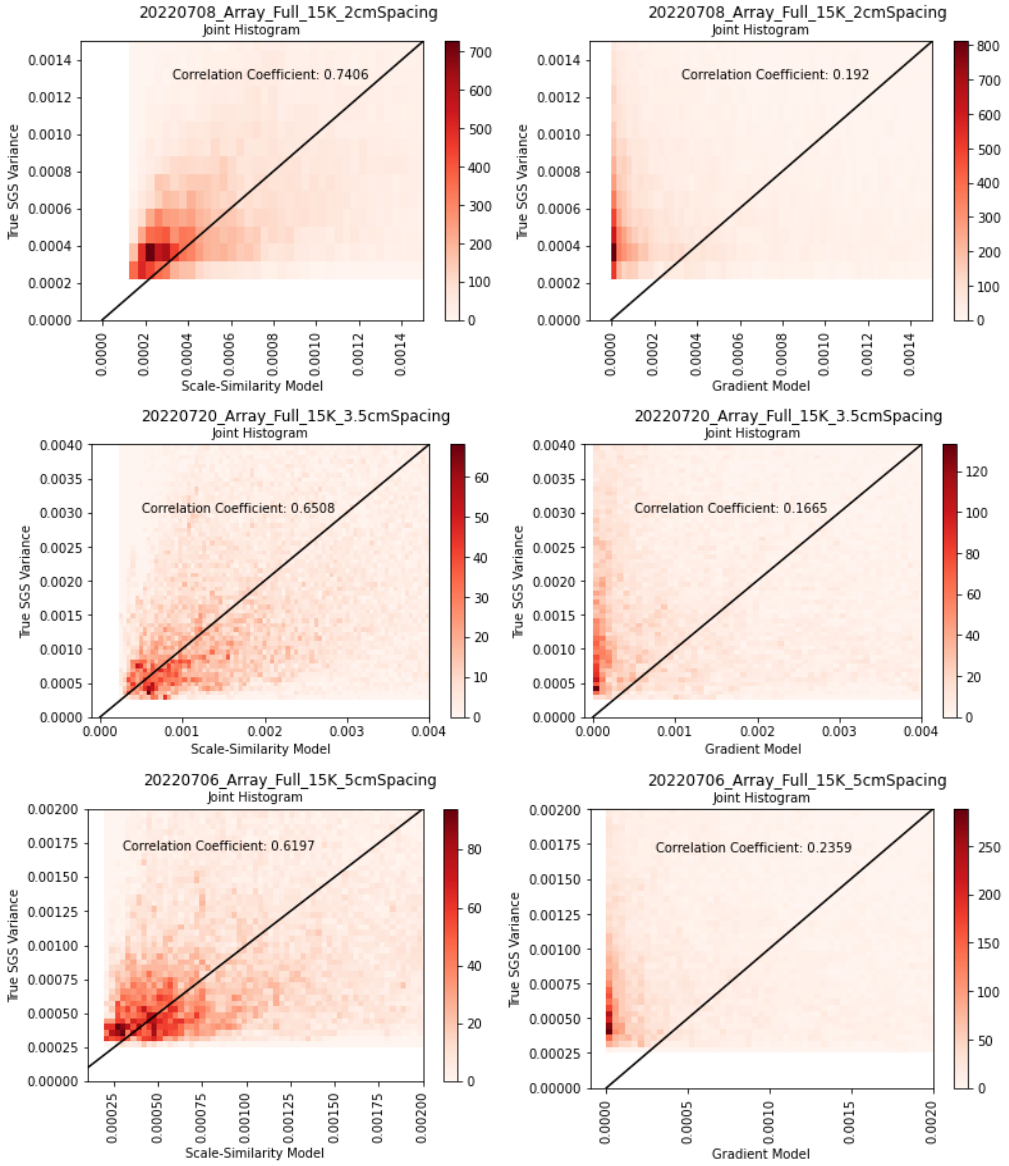

Figure 21. Joint-histogram plots of 15K measurements at three different widths. On the Left is the joint-histogram plot of the calculated variance versus the scale-similarity modeled variance. On the right is the joint-histogram plot of the calculated variance versus the Gradient modeled variance. Gaussian-filter was used for all plots shown. Data taken on the 7th was replaced with data taken on the 20th due to the data taken on the 7th being in the updraft instead of the downdraft.

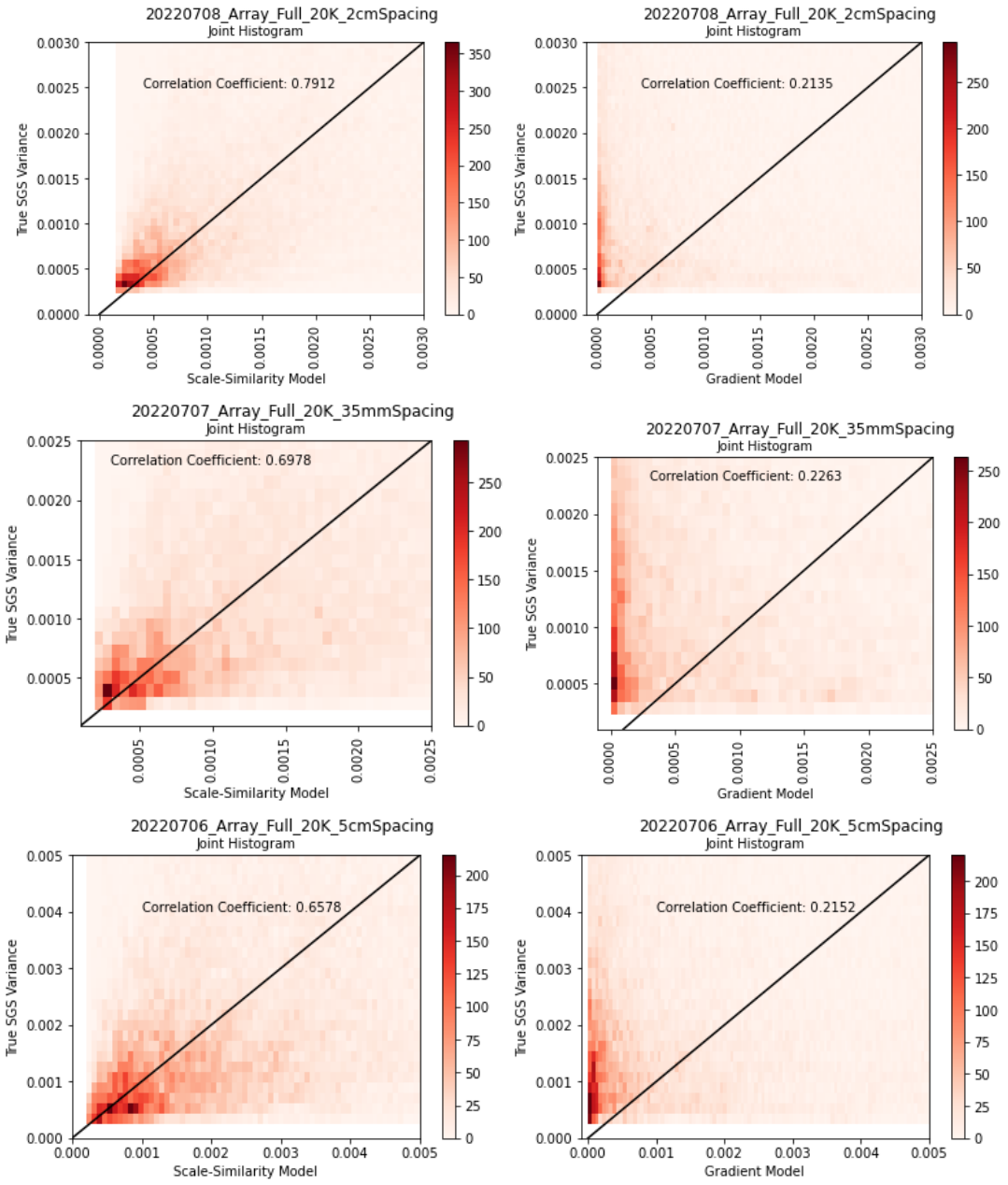

Figure 22. Joint-histogram plots of 20K measurements at three different widths. On the Left is the joint-histogram plot of the calculated variance versus the scale-similarity modeled variance. On the right is the joint-histogram plot of the calculated variance versus the Gradient modeled variance. Gaussian-filter was used for all plots shown.

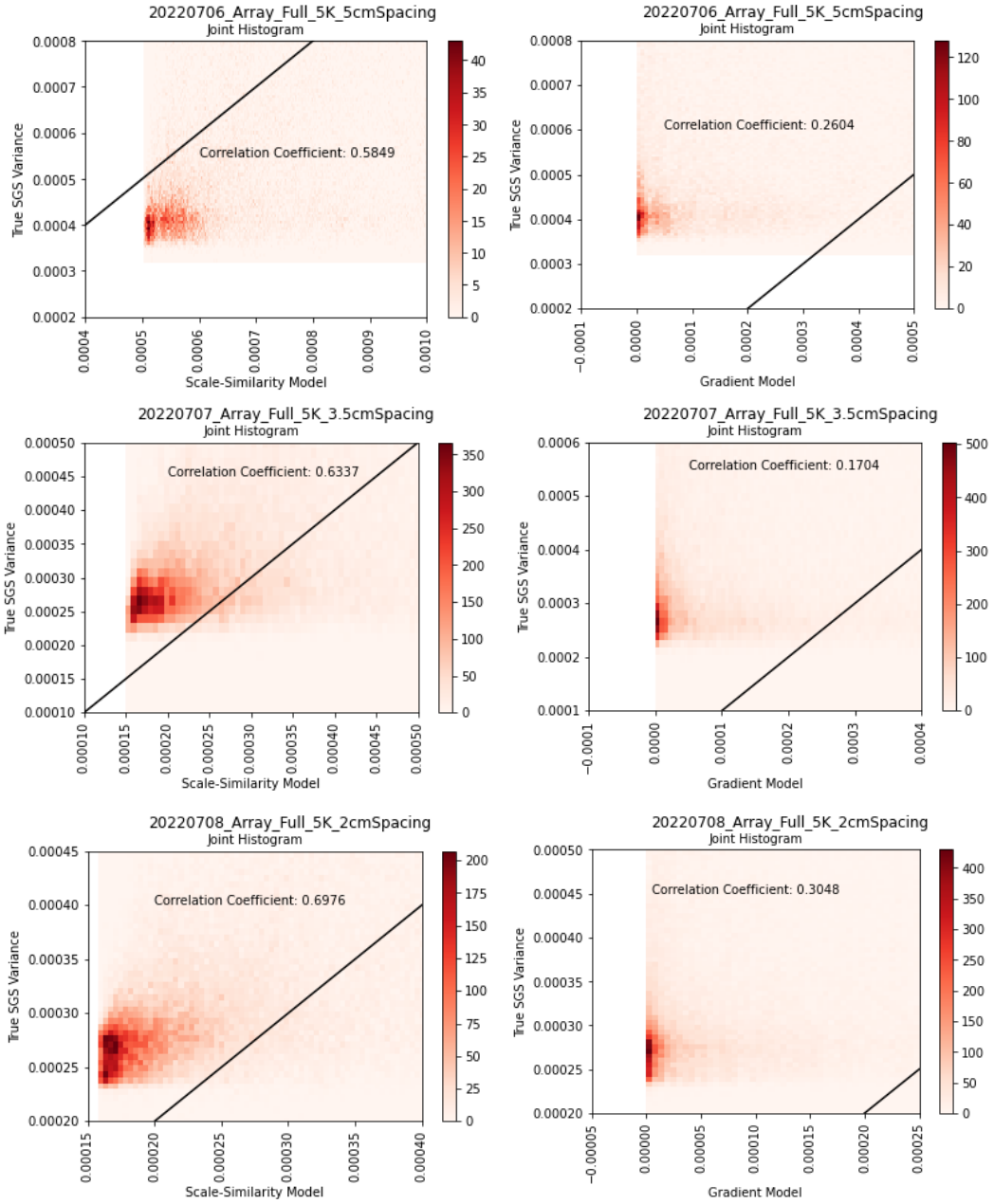

Figure 23. Joint-histogram plots of 5K measurements at three different widths. On the Left is the joint-histogram plot of the calculated variance versus the scale-similarity modeled variance. On the right is the joint-histogram plot of the calculated variance versus the Gradient modeled variance. Box-filter was used for all plots shown.

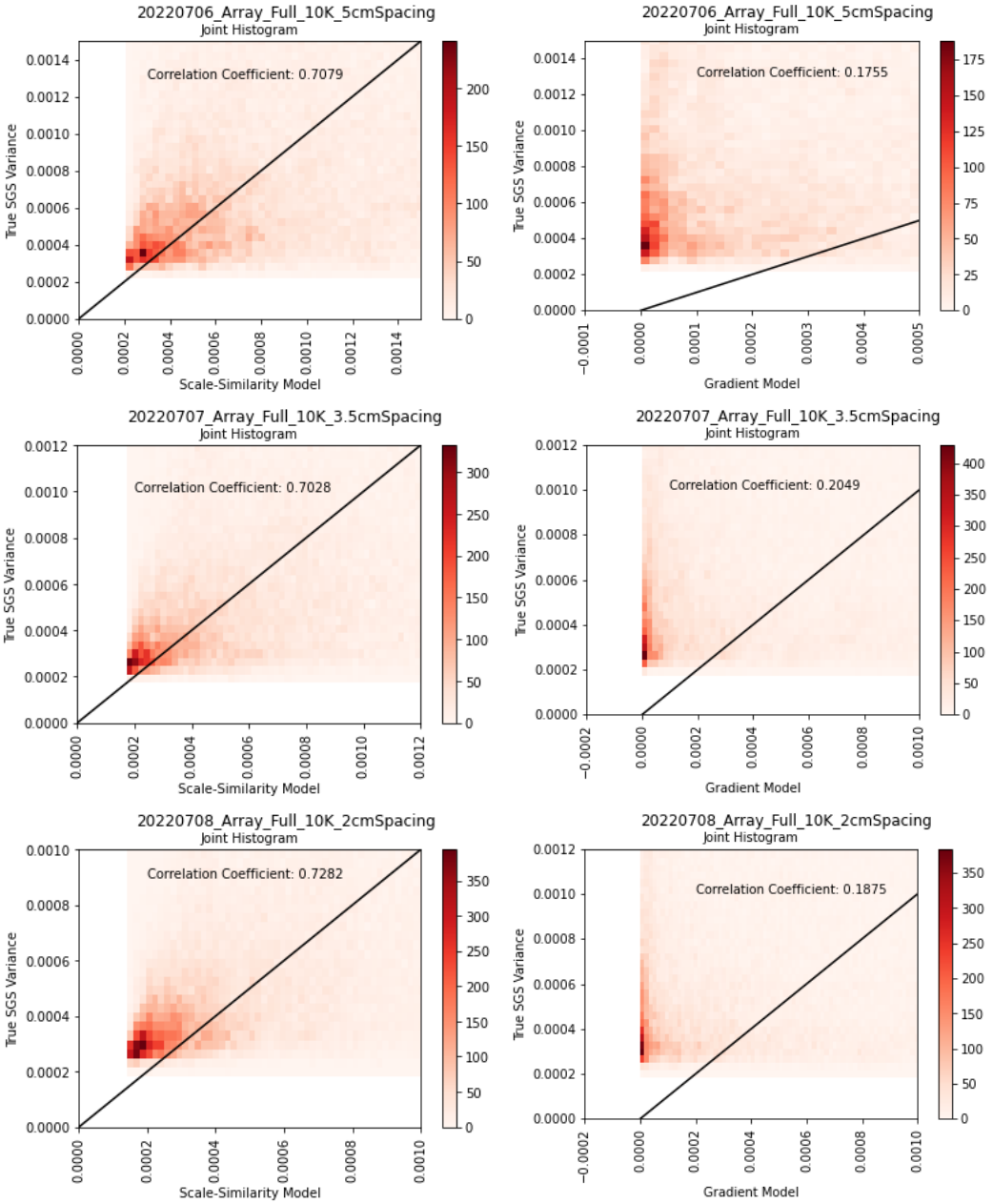

Figure 24. Joint-histogram plots of 10K measurements at three different widths. On the Left is the joint-histogram plot of the calculated variance versus the scale-similarity modeled variance. On the right is the joint-histogram plot of the calculated variance versus the Gradient modeled variance. Box-filter was used for all plots shown.

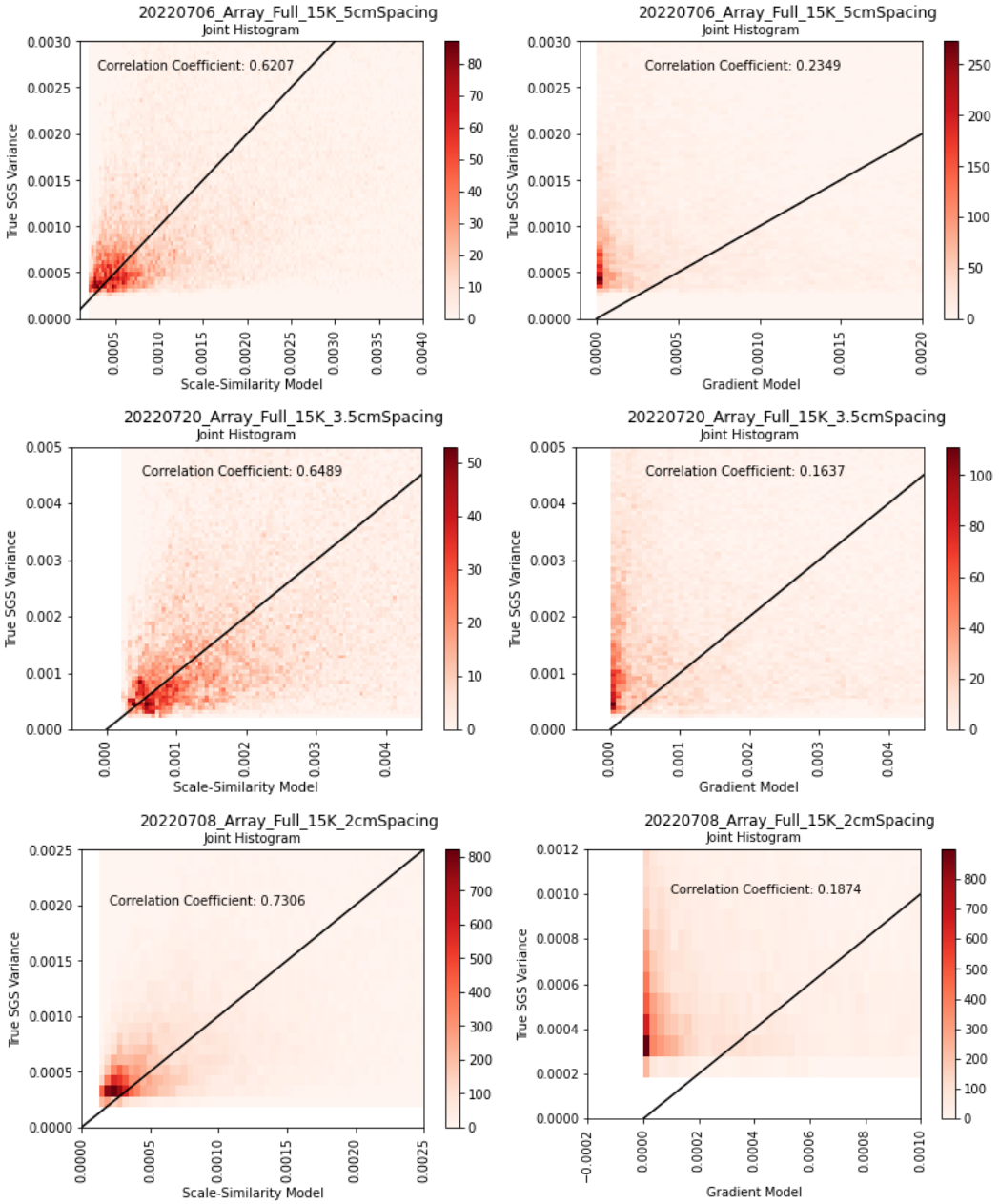

Figure 25. Joint-histogram plots of 15K. On the Left is the joint-histogram plot of the calculated variance versus the scale-similarity modeled variance. On the right is the joint-histogram plot of the calculated variance versus the Gradient modeled variance. Box-filter was used for all plots shown. Data taken on the 7th was replaced with data taken on the 20th due to the data taken on the 7th being in the updraft instead of the downdraft.

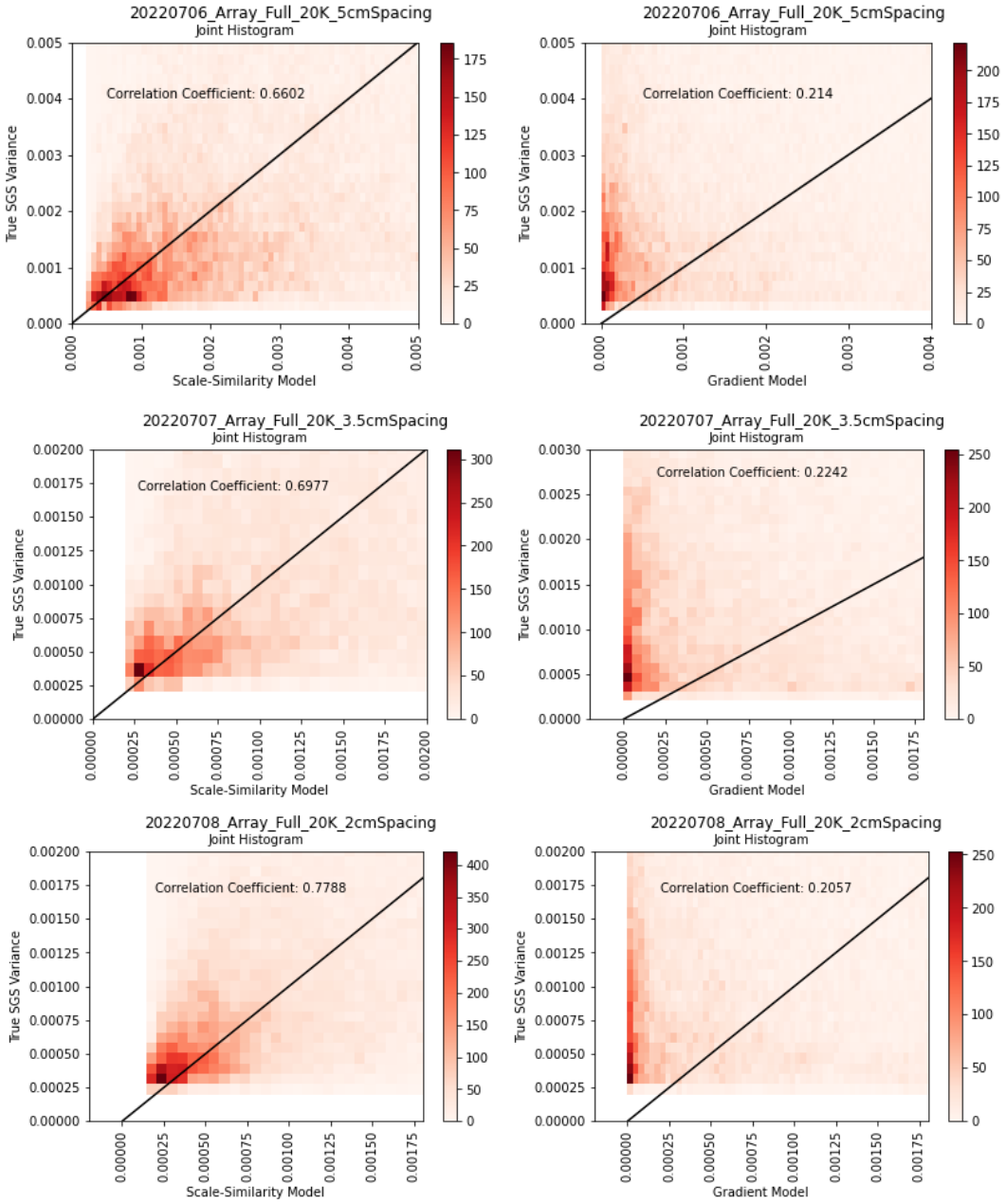

Figure 26. Joint-histogram plots of 20K measurements at three different widths. On the Left is the joint-histogram plot of the calculated variance versus the scale-similarity modeled variance. On the right is the joint-histogram plot of the calculated variance versus the Gradient modeled variance. Box-filter was used for all plots shown.

Figures 19-26 also show the correlation coefficient for each τ and $\tau_{calculated}$. These coefficients are also shown in table 2 and figure 27. It does appear that the scale similarity model more closely resembles the statistics of $\tau_{calculated}$ from the raw data, and scale similarity model also has much larger correlation coefficients.

Both the histograms and the joint histograms suggest that the scale similarity model is a strong model for the true subgrid scale variance. But the Gradient model under-represents the energy and momentum contained within the subgrid scale turbulence.

3.3: Interpretation

The scale-similarity model has much higher correlation coefficients than the Gradient model. In all cases, what filter was used appeared to have very little, if any, impact. Figure 27 shows a comparison of the correlation coefficients. For the scale similarity model, there was a slight trend between the temperature difference and the model's accuracy. This suggests that the model may do better in higher Reynold's number situations. This same trend can be seen in the histograms; the scale similarity model more closely follows the true subgrid scale variance at higher temperatures and follows it much less at the 5K temperature difference. If this model is better at representing turbulent flow than laminar flow, it would make sense that it is a more accurate model at higher Reynolds number. Though nothing can be said for sure, it is promising that this model may show better results in more turbulent

situations. Other than this, the only variable which consistently impacted the correlation coefficient is which model, which version of τ, was used.

Correlation Coefficients					
		Scale-Similarity Model		Gradient Model	
δx	δ Temperature	Box-Filter	Gaussian- Filter	Box-Filter	Gaussian- Filter
2 cm	5K	0.6976	0.7003	0.3048	0.3089
	10K	0.7282	0.7421	0.1875	0.1943
	15K	0.7306	0.7406	0.1874	0.192
	20K	0.7788	0.7912	0.2057	0.2135
3.5 cm	5K	0.6337	0.6307	0.1704	0.1721
	10K	0.7028	0.7051	0.2049	0.2062
	15K	0.6489	0.6508	0.1637	0.1665
	20K	0.6977	0.6978	0.2242	0.2263
5 cm	5K	0.5849	0.5827	0.2604	0.2606
	10K	0.7079	0.7075	0.1755	0.1763
	15K	0.6207	0.6197	0.2349	0.2359
	20K	0.6602	0.6578	0.214	0.2152

Table 2. Correlation coefficients between τ and $\tau_{calculated}$. Correlation coefficients shown for all three spacings, all four temperature gradients, both models and both filters.

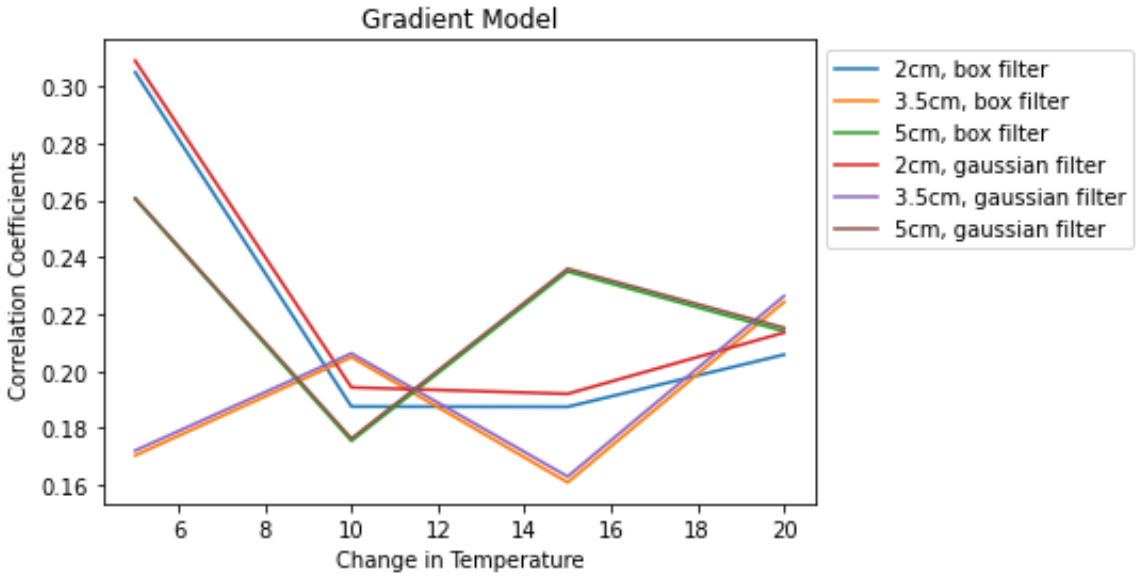

(a)

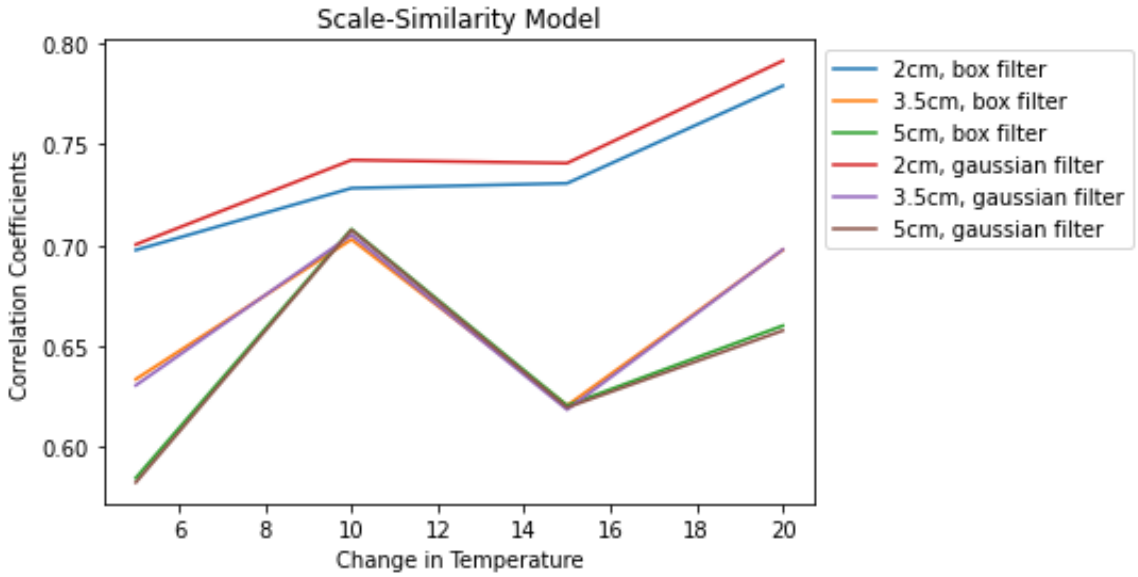

(b)

Figure 27. Correlation Coefficients for Gradient model (a) and scale-similarity model (b) plotted against temperature difference between the floor and the ceiling in degrees Celsius. Plots show all three spacings in both filters.

It can be seen on figure 27 and table 2 that which filter is used when the thermistors were spaced 3.5cm and 5cm apart has almost no impact. Minimal impact can be seen when the thermistors are spaced 2cm apart, slightly favoring the Gaussian filter in both models. It is possible this is because the smaller the grid spacing, the greater impact the small differences between the filters will have. But more variations would have to be tested to say this for sure.

It appears which filter is used has negligible impact on the efficiency of the model. There does not appear to be any patterns in the correlation due to changes in spacing or temperature difference. Scale-similarity shows mild patterns between higher correlation with smaller spacing width and higher correlation with higher temperature change. The patterns are mild and more testing would need to be attempted to verify either of these correlations.

Chapter 4

Conclusion

Turbulent flow is characterized by fluids undergoing irregular flow patterns, which induces mixing and pseudo-chaotic behavior. Turbulent flow is characterized by swirling eddies feeding off of and interacting with each other. Often, when turbulence is studied, it is done so in reference to these eddies. Because of this, researching and modeling turbulent flow is generally focused on understanding eddies' behavior.

In the case of turbulence induced in the Pi chamber at Michigan Tech, the largest of these eddies has a diameter roughly the size of the vertical parameter of the chamber. This large-scale eddy is referred to as the LSC (large scale circulation) within the Pi Chamber. The direction of this LSC was found by taking histogram plots of the data collected by the thermistors and RTDs (see figure 6). The thermistor array was stationed in the downdraft of the LSC for the cleanest turbulent data.

The Navier-Stokes equations are equations based on conservation of mass, Newton's second law, the assumption that the fluid is non-compressible and the assumption that stress in the fluid is the sum of the diffusing viscous term and pressure term. In order to use the Navier-Stokes equations, the fluid must be treated as a continuous substance, ignoring the properties of individual molecules. Although DNS (direct numerical simulation) can be used to simulate systems, it is computationally expensive. Generally, LES (large eddy simulation) is favored.

For LES, turbulence is broken into grid-scale simulated flow and subgrid-scale modeled flow (see figure 1). Larger eddies are simulated using the Navier-Stokes equations while smaller eddies and forms of motion are modeled as the variable τ (see equation 2). In this research, the turbulence measured was divided according to the size of the eddies in frequency space. Two filter types were used: box filter and Gaussian filter. The subgrid-scale turbulence was then simulated using a variation of the Navier-Stokes equations which takes the statistics of the modeled flow into account (see equation 2). LES is computationally reasonable and gives valuable and reliable results. However, its accuracy is dependent on the accuracy of the subgrid-scale model, τ.

In this research, we used two models. The first model used was the scale-similarity model (see equation 10) which can be obtained by using the zeroth-order expansion of the deconvolution operator (Sagaut, 2001). The other model being investigated is the Gradient model, which was designed to be a workable model in many different situations (see equation 12). Because the gradient model was being studied, the thermistor array was required to have both seven thermistors on the first row and three on the second (see figure 5 and figure 9).

Although both of these models are based on physical understanding of fluid mechanics, there are variables and coefficients in the models which remain unknown. To determine these, data was gathered in the Pi Chamber at Michigan Tech. Through this a priori testing, the model was then calculated. The calculation

of these coefficients is shown in equation 11 and equation 13. A single value of C is found for every temperature difference, change in filter width, both filter types and both models. This gives 48 calculated coefficients in all. The values for these model coefficients are shown in table 1 and figure 10.

These coefficients were then inserted back into equation 10 and equation 12. The calculated models were compared to the original $\tau_{calculated}$, calculated by equation 9. A correlation coefficient was calculated for $\tau_{calculated}$ and the scaled models. These values are shown in table 2 and figure 27.

In all spacings and the higher temperature differences, the scale similarity model appears to have performed well with correlation coefficients between 0.6 and 0.8. The histograms of the scale similarity model closely resembled the true subgrid scale variance, particularly at high temperature differences. The joint histograms also show that the scale similarity model is a good statistical representation of the true subgrid scale variance by showing a strong one-to-one correlation across many values. These are promising results for LES research in cloud turbulence.

The Gradient model did not perform as well. The histograms and joint histograms suggested that it modeled the momentum in the system lower than the actual variance, and the correlation coefficients were around 0.2. This is a bit surprising because the Gradient model tends to be more widely used than the scale similarity

model. However, a correlation coefficient of 0.2 is not so low in the turbulence community as to invalidate it as a model.

No prominent patterns were observed between the correlation coefficient between τ and $\tau_{calculated}$ and either the temperature difference or the spacing of the array. Scale-similarity shows mild patterns between higher correlation with smaller spacing width and higher correlation with higher temperature change. But the patterns are small. To know for sure, more tests would have to be run.

This research was done in the hopes that this could help the scientific community better establish models for use in LES in saturated air. There is a possible correlation between temperature turbulence in saturated air and turbulent fluctuations of supersaturation (Chandrakar, 2020). Accurate models of turbulent temperature fluctuations in saturated air will greatly improve the community's ability to create models for LES for cloud formation and behavior.

Much of precipitation in saturated conditions is formed through collision and coalescence. These interactions between droplets are governed by the turbulence within the cloud. Models showing the turbulent behavior of temperature and saturation in saturated conditions are necessary for understanding and modeling clouds and precipitation.

For future work, these models need a posteriori testing in various experiments. To do this, experiments would be run in a controllable chamber such as the Pi Chamber at Michigan Tech. An LES would be computationally built using the models designed in this research with the same initial conditions as the experiment. The turbulence simulated by the LES would then be compared to the turbulence measured by the experiment. How well the LES simulates the measured turbulence would be the actual test in how well the models model the subgrid scale turbulence.

A posteriori tests must be performed on the models to know for sure how well they perform in LES for actual turbulence. However, the results that were found in this research are promising. The scale-similarity model shows correlation coefficients between 0.55 and 0.8. For LES models of turbulence, these are quite high. The results found in this paper appear to be very promising for future turbulent research.

References Cited

Anderson, J. C., Thomas, S., Prabhakaran, P., Shaw, R. A., and Cantrell, W.: Effects of the large-scale circulation on temperature and water vapor distributions in the Π Chamber, Atmos. Meas. Tech., 14, 5473–5485, https://doi.org/10.5194/amt-14-5473-2021, 2021.

BARDINA, J., et al. “Improved Subgrid-Scale Models for Large-Eddy Simulation.” *13th Fluid and PlasmaDynamics Conference*, 1980, https://doi.org/10.2514/6.1980-1357.

Barrett, P. A., Blyth, A., Brown, P. R. A., and Abel, S. J.: The structure of turbulence and mixed-phase cloud microphysics in a highly supercooled altocumulus cloud, Atmos. Chem. Phys., 20, 1921–1939, https://doi.org/10.5194/acp-20-1921-2020, 2020.

Besnard D.C., Harlow F.H., Rauenzahn R.M., Zemach C. (1996). Spectral transport model for turbulence. Theoret. Comput. Fluid Dyn. 8: 1–35

Bhushan S., Warsi Z.U.A. (2005). Large eddy simulation of turbulent channel flow using an algebraic model. Int. J. Numer. Methods Fluids 49: 489–519

Bodenschatz, E., et al. “Can We Understand Clouds without Turbulence?” *Science*, vol. 327, no. 5968, 2010, pp. 970–971., https://doi.org/10.1126/science.1185138.

Brinkop, S., & Roeckner, E. (1995). Sensitivity of a general circulation model to parameterizations of cloud—Turbulence interactions in the atmospheric boundary layer. *Tellus A*, 47(2), 197– 220. https://doi.org/10.3402/tellusa.v47i2.11501

Cambon C., Jeandel D., Mathieu J. (1981). Spectral modelling of homogeneous non-isotropic turbulence. J. Fluid Mech. 104: 247–262

Chandrakar, K. K., et al. “Influence of Turbulent Fluctuations on Cloud Droplet Size Dispersion and Aerosol Indirect Effects.” *Journal of the Atmospheric Sciences*, vol. 75, no. 9, 2018, pp. 3191–3209., https://doi.org/10.1175/jas-d-18-0006.1

Chandrakar, K., Cantrell, W., Krueger, S., Shaw, R., & Wunsch, S. (2020). Supersaturation fluctuations in moist turbulent Rayleigh–Bénard convection: A two-scalar transport problem. *Journal of Fluid Mechanics, 884*, A19. doi:10.1017/jfm.2019.895

Chang, K., Bench, J., Brege, M., Cantrell, W., Chandrakar, K., Ciochetto, D., et al. (2016). A laboratory facility to study gas–aerosol–cloud interactions in a turbulent environment: The π chamber. *Bulletin of the American Meteorological Society*, 97(12), 2343– 2358. https://doi.org/10.1175/bams-d-15-00203.1

Chang, K., and Coauthors, 2016: A Laboratory Facility to Study Gas–Aerosol–Cloud Interactions in a Turbulent Environment: The Π Chamber. *Bull. Amer. Meteor. Soc.*, **97**, 2343–2358, https://doi.org/10.1175/BAMS-D-15-00203.1.

Chaouat B. (2001). Simulations of channel flows with effects of spanwise rotation or wall injection using a Reynolds stress model. J. Fluid Eng. ASME, 123: 2–10

Chaouat, B., Schiestel, R.: A new partially integrated transport model for subgrid-scale stresses and dissipation rate for turbulent developing flows. Phys. Fluids 17(6), (2005)

Chaouat, B., Schiestel, R. From single-scale turbulence models to multiple-scale and subgrid-scale models by Fourier transform. *Theor. Comput. Fluid Dyn.* 21, 201–229 (2007). https://doi.org/10.1007/s00162-007-0044-3

Clark T.T., Zemach C. (1995). A spectral model applied to homogeneous turbulence. Phys. Fluids 7(7): 1674–1694

Córcoles, J.I., Díaz-Heras, M., Fernández-Torrijos, M., and Almendros-Ibáñez, J.A., 2023, "Flow and heat transfer analysis of a gas-particle fluidized dense suspension in a tube for CSP applications" Renewable Energy 09601481

Deardorff, J.W. Stratocumulus-capped mixed layers derived from a three-dimensional model.*Boundary-Layer Meteorol* 18, 495–527 (1980). https://doi.org/10.1007/BF00119502

Desai, N., K. K. Chandrakar, K. Chang, W. Cantrell, and R. A. Shaw, 2018: Influence of Microphysical Variability on Stochastic Condensation in a Turbulent Laboratory Cloud. *J. Atmos. Sci.*, **75**, 189–201, https://doi.org/10.1175/JAS-D-17-0158.1.

Devenish, B. J., et al. “Droplet Growth in Warm Turbulent Clouds.” *Quarterly Journal of the Royal Meteorological Society*, vol. 138, no. 667, 2012, pp. 1401–1429., https://doi.org/10.1002/qj.1897.

Ding, Yuan, Pang, Bi-yu, Yan, Bo-wen, Wang, Yi-qian, Chen, Yu-xuan, and Qian, Yue-hong, 2023, "A Liutex-based subgrid stress model for large-eddy simulation" Journal of Hydrodynamics 1878-0342

Du, Qiang, Xie, Yaguang, Wang, Zhicheng, Jiang, Xiaomo, and Xie, Lei, 2023, "An entropy viscosity method for large eddy simulation of turbulent thermal flow in a rotor–stator cavity" Physics of Fluids Vol. 35, No. 3, pp 035126, 1089-7666

Gao, Jinjin, Liu, Han, Lee, Jiyong, Zheng, Yuan, Guala, Michele, and Shen, Lian, 2021, "Large-eddy simulation and Co-Design strategy for a drag-type vertical axis hydrokinetic turbine in open channel flows" Renewable Energy 09601481

Germano, U. Piomelli, P. Moin, and W. H. Cabot, “ A dynamic subgrid-scale eddy viscosity model,” Phys. Fluids A **3**, 1760 (1991). https://doi.org/10.1063/1.857955

Germano, M.: From RANS to DNS: toward a bridging model. In: Voke, P., Sandham, N.D., Kleiser, L. (eds) Direct and Large-Eddy simulation III, Ercoftac Series, Vol. 7 pp. 225-235. Kluwer (1999)

Grabowski, Wojciech W., and Lian-Ping Wang. “Growth of Cloud Droplets in a Turbulent Environment.” *Annual Review of Fluid Mechanics*, vol. 45, no. 1, 2013, pp. 293–324., https://doi.org/10.1146/annurev-fluid-011212-140750.

Grabowski, W. W., 2020: Comparison of Eulerian Bin and Lagrangian Particle-Based Schemes in Simulations of Pi Chamber Dynamics and Microphysics. *J. Atmos. Sci.*, **77**, 1151–1165, https://doi.org/10.1175/JAS-D-19-0216.1.

Hamba F. (2001). An attempt to combine large eddy simulation with the k−ε model in a channel-flow calculation. Theoret. Comput. Fluid Dyn. 14: 323–336

Hanjalic, K., Launder, B.E., Schiestel, R.: Multiple time-scale concepts in turbulence transport modeling. In: Turbulent Shear Flows, 2nd edn. Springer (1980)

Haochen Li, Yaomin Zhao, Jianchun Wang, Richard D. Sandberg. (2021) Data-driven model development for large-eddy simulation of turbulence using gene-expression programing. *Physics of Fluids* **33**:12, 125127. Online publication date: 20-Dec-2021.

Hervé Henry. (2023) Numerical study of buoyancy induced arrest of viscous coarsening. *Physics of Fluids* **35**:1, 013301. Online publication date: 3-Jan-2023.

Jakirlic S., Hanjalic K. (2002). A new approach to modelling near-wall turbulence energy and stress dissipation. J. Fluid Mech. 459: 139–166

Jeandel D., Brison J.F., Mathieu J. (1978). Modeling methods in physical and spectral space. Phys. Fluids 21(2): 169–182

Kairzhan Karzhaubayev, Lian-Ping Wang, Dauren Zhakebayev. (2022) An efficient parallel spectral code for 3D periodic flow simulations. *SoftwareX* **20**, 101244. Online publication date: 1-Dec-2022.

Katopodes, Nikolaos D. *Free-Surface Flow*. Butterworth-Heinemann, an Imprint of Elsevier, 2019.

Katz, Sarah, Caiazzo, Alfonso, Moreau, Baptiste, Wilbrandt, Ulrich, Brüning, Jan, Goubergrits, Leonid, and John, Volker, 2023, "Impact of turbulence modeling on the simulation of blood flow in aortic coarctation" International Journal for Numerical Methods in Biomedical Engineering 2040-7947

Keating, A., Piomelli, U., Balaras, E., & Kaltenbach, H. J. (2004). *A priori*and*a posteriori*tests of inflow conditions for large-eddy simulation. *Physics of Fluids*, *16*(12), 4696–4712. https://doi.org/10.1063/1.1811672

Kleissl, Jan, et al. “On the Magnitude and Variability of Subgrid-Scale Eddy-Diffusion Coefficients in the Atmospheric Surface Layer.” *Journal of the Atmospheric Sciences*, vol. 60, no. 19, 2003, pp. 2372–2388., https://doi.org/10.1175/1520-0469(2003)060<2372:otmavo>2.0.co;2.

Koren, Márton and Kristóf, Gergely, 2023, "Investigation of the accuracy of the transient wind forcing model applied for a shear-driven LES" Journal of Wind Engineering and Industrial Aerodynamics Vol. 236, pp 105363, 01676105

Launder B.E. (1989). Second moment closure: Present and future? Int. Heat Fluid Flow 20(4): 282–300

Lavely, Adam, Lorenz, Ralph, and Schmitz, Sven, 2021, "Large-Eddy Simulation of Titan’s near-surface atmosphere: Convective turbulence and flow over dunes with application to Huygens and Dragonfly" Icarus Vol. 357, pp 114229, 00191035

Leschziner M.A., Drikakis D. (2002). Turbulence modelling and turbulent-flow computation in aeronautics. Aeronaut. J. 106: 349–384

Lesieur M., Métais O. (1996). New trends in large-eddy simulations of turbulence. Ann. Rev. J. Fluid Mech. 28: 45–82

Lesieur, M., Métais, O., Comte, P.: Large-Eddy Simulations of Turbulence. Cambridge University Press, (2005)

Lian, Yuan and Richardson, Mark I., 2023, "Unstructured grid dynamical modeling of planetary atmospheres using planetMPAS: The influence of the rigid lid, computational efficiency, and examples of Martian and Jovian application" Planetary and Space Science pp 105663, 00320633

Liu N.S., Shih T.H. (2006). Turbulence modeling for very large-eddy simulation. AIAA J. 44(4): 687–697

Lorenz, E. N., 1963: Deterministic Nonperiodic Flow. *J. Atmos. Sci.*, **20**, 130–141, https://doi.org/10.1175/1520-0469(1963)020<0130:DNF>2.0.CO;2.

Ma, J. *et al. “*A low Reynolds number variant of partially-averaged Navier-Stokes model for turbulence” Int. J. Heat Fluid Flow (2011)

Meneveau, Charles, and Joseph Katz. “Scale-Invariance and Turbulence Models for Large-Eddy Simulation.” *Annual Review of Fluid Mechanics*, vol. 32, no. 1, 2000, pp. 1–32., https://doi.org/10.1146/annurev.fluid.32.1.1.

Mohamed Y. Hashim, Jonggeun Bae, Jeekeun Lee. (2023) Experimental and numerical studies of the effects of the contraction ratios on the swirling flow characteristics of the model combustor outlet in lean gas turbines. *Applied Thermal Engineering* **218**, 119371. Online publication date: 1-Jan-2023.

Muñoz-Esparza, Domingo, Sharman, Robert D., and Trier, Stanley B., 2020, "On the Consequences of PBL Scheme Diffusion on UTLS Wave and Turbulence Representation in High-Resolution NWP Models" Monthly Weather Review Vol. 148, No. 10, pp 4247, 1520-0493

Niedermeier, Dennis and Chang, Kelken and Cantrell, Will and Chandrakar, Kamal Kant and Ciochetto, David and Shaw, Raymond A. (2018). Observation of a link between energy dissipation rate and oscillation frequency of the large-scale circulation in dry and moist Rayleigh-B\'enard turbulence, https://link.aps.org/doi/10.1103/PhysRevFluids.3.083501

Pope, Steven B. *Turbulent Flows*. Cambridge University Press, 2000.

Porté-Agel, Fernando, et al. “A Priori Field Study of the Subgrid-Scale Heat Fluxes and Dissipation in the Atmospheric Surface Layer.” *Journal of the Atmospheric Sciences*, vol. 58, no. 18, 2001, pp. 2673–2698., https://doi.org/10.1175/1520-0469(2001)058<2673:apfsot>2.0.co;2.

Potsis, Theodore, Tominaga, Yoshihide, and Stathopoulos, Ted, 2023, "Computational wind engineering: 30 years of research progress in building structures and environment" Journal of Wind Engineering and Industrial Aerodynamics Vol. 234, pp 105346, 01676105

Razi, P., Ramaprabhu, P., Tarey, P., Muglia, M., and Vermillion, C., 2022, "A low-order wake interaction modeling framework for the performance of ocean current turbines under turbulent conditions" Renewable Energy 09601481

Rubinstein R., Clark T.T. (2004). A generalized Heisenberg model for turbulent spectral dynamics. Theoret. Comput. Fluid Dyn. 17: 249–272

Rumsey C.L., Gatski T.B. (2001). Recent turbulence model advances applied to multielement airfoil computations. J. Aircraft 38(5): 904–910

Sagaut, Pierre. “Coupling with Passive/Active Scalar.” *Large Eddy Simulation for Incompressible Flow*, Third Edition ed., Springer, 2001.

Santacreu, J.V. Gutiérrez and Rojas-Medar, M.A., 2023, "On the approximation of turbulent fluid flows by the Navier–Stokes-α equations on bounded domains" Physica D: Nonlinear Phenomena pp 133724, 01672789

Schlipf, David, et al. (2011) Testing of frozen turbulence hypothesis for wind turbine applications with a scanning LIDAR system. *OPUS - Publication Server of the University of Stuttgart*. http://dx.doi.org/10.18419/opus-3915

Shaw, Raymond A. “Particle-Turbulence Interactions in Atmospheric Clouds.” *Annual Review of Fluid Mechanics*, vol. 35, no. 1, 2003, pp. 183–227., https://doi.org/10.1146/annurev.fluid.35.101101.161125.

Siebert, H., and R. A. Shaw, 2017: Supersaturation Fluctuations during the Early Stage of Cumulus Formation. *J. Atmos. Sci.,* **74**, 975-988

da Silva, Carlos B., Hunt, Julian C.R., Eames, Ian, Westerweel, Jerry. *Annual Review of Fluid Mechanics,* Vol. 46:567-590 (2014) https://doi.org/10.1146/annurev-fluid-010313-141357

Simone Ferrari, Riccardo Rossi, Annalisa Di Bernardino. (2022) A Review of Laboratory and Numerical Techniques to Simulate Turbulent Flows. *Energies* **15**:20, 7580. Online publication date: 14-Oct-2022.

SMAGORINSKY, J., 1963: GENERAL CIRCULATION EXPERIMENTS WITH THE PRIMITIVE EQUATIONS. *Mon. Wea. Rev.*, **91**, 99–164, https://doi.org/10.1175/1520-0493(1963)091<0099:GCEWTP>2.3.CO;2.

Spalart P.R. (2000). Strategies for turbulence modelling and simulations. Int. J. Heat Fluid Flow 21: 252–263

Speziale C.G. (1991). Analytical methods for the development of Reynolds-stress closures in turbulence. Ann. Rev. Fluid Mech. 23: 107–157

SULLIVAN, P., HORST, T., LENSCHOW, D., MOENG, C., & WEIL, J. (2003). Structure of subfilter-scale fluxes in the atmospheric surface layer with application to large-eddy simulation modelling. *Journal of Fluid Mechanics, 482*, 101-139. doi:10.1017/S0022112003004099

Sullivan (2018). Using HATS Databases to Evaluate Subfilter-Scale Rate Equations for LES. *Mesoscale & Microscale Meteorology Division National Center for Atmospheric Research, Boulder, CO.*

T E G Nicholas, J Omotani, F Riva, F Militello, B Dudson. (2022) Comparing two- and three-dimensional models of scrape-off layer turbulent transport. *Plasma Physics and Controlled Fusion* **64**:9, 095001. Online publication date: 14-Jul-2022.

Temel, Orkun, Senel, Cem Berk, Porchetta, Sara, Muñoz-Esparza, Domingo, Mischna, Michael A., Van Hoolst, Tim, van Beeck, Jeroen, and Karatekin, Özgür, 2021, "Large eddy simulations of the Martian convective boundary layer: Towards developing a new planetary boundary layer scheme" Atmospheric Research Vol. 250, pp 105381, 01698095

Thomas, S., Ovchinnikov, M., Yang, F., van der Voort, D., Cantrell, W., Krueger, S. K., & Shaw, R. A.(2019). Scaling of an atmospheric model to simulate turbulence and cloud microphysics in the Pi Chamber. *Journal of Advances in Modeling Earth Systems*, 11(7), 1981– 1994. https://doi.org/10.1029/2019ms001670

Wyngaard JC, Tennekes H (1962) Measurements of the small-scale structure of turbulence at moderate Reynolds numbers. Phys Fluids 13:1962–1969. https://doi.org/10.1063/1.1693192

Wyngaard, J. C., and O. R. Coté, 1971: The Budgets of Turbulent Kinetic Energy and Temperature Variance in the Atmospheric Surface Layer. *J. Atmos. Sci.*, **28**, 190–201, https://doi.org/10.1175/1520-0469(1971)028<0190:TBOTKE>2.0.CO;2.

Wyngaard, “Atmospheric Turbulence.” *Annual Review of Fluid Mechanics*, 1992, https://doi.org/10.1146/annurev.fl.24.010192.001225

Xing, Fengda and Lei, Chengwang, 2022, "A large eddy simulation of flow over a circular cylinder with circumferential triangular riblets: Effects of spanwise coverage ratio" Ocean Engineering Vol. 263, pp 112439, 00298018

Xue, L., and Coauthors, 2022: Progress and Challenges in Modeling Dynamics–Microphysics Interactions: From the Pi Chamber to Monsoon Convection. *Bull. Amer. Meteor. Soc.*, **103**, E1413–E1420, https://doi.org/10.1175/BAMS-D-22-0018.1.

Yan, Longlong, Gao, Bo, Ni, Dan, Zhang, Ning, and Zhou, Wenjie, 2023, "Wavelet analysis of mixing layers with emphasis on intermittency and cavitation events" Ocean Engineering Vol. 275, pp 114088, 00298018

Yoshizawa A. (1982). A statistically-derived subgrid model for the large-eddy simulation of turbulence. Phys. Fluids 25(9): 1532–1538

Yoshizawa A. (1984). Statistical analysis of the deviation of the Reynolds stress form its eddy-viscosity representation. Phys. Fluids, 27(6): 1377–1387